

LARGE SCALE MOTIONS OF NEPTUNE'S
BOW SHOCK: EVIDENCE FOR CONTROL OF THE
SHOCK POSITION BY THE ROTATION PHASE
OF NEPTUNE'S MAGNETIC FIELD

by

Iver H. Cairns¹, Charles W. Smith², William S. Kurth¹,
Donald A. Gurnett¹, and Stewart L. Moses³

January 1991

¹Dept. of Physics and Astronomy, University of Iowa, Iowa City, IA 52242

²Bartol Research Institute, University of Delaware, Newark, DE 19716

³TRW Space and Technology Group, One Space Park, Redondo Beach, CA 90278

Large Scale Motions of Neptune's Bow Shock: Evidence for Control of the Shock Position by the Rotation Phase of Neptune's Magnetic Field

Iver H. Cairns¹, Charles W. Smith², William S. Kurth¹, Donald A. Gurnett¹, and Stewart Moses³.

¹ Department of Physics and Astronomy, University of Iowa, Iowa City, IA 52242, USA.

² Bartol Research Institute, University of Delaware, Newark, DE 19716, USA.

³ TRW Space and Technology Group, 1 Space Park, Redondo Beach, CA 90278, USA.

Abstract

The Voyager 2 spacecraft observed high levels of Langmuir waves before the inbound crossing of Neptune's bow shock, thereby signifying magnetic connection to the bow shock. The Langmuir waves occurred in multiple bursts throughout two distinct periods separated by an 85 minute absence of wave activity. We use the times of onsets, peaks and disappearances of the waves, together with the magnetic field direction and spacecraft position, to perform a "remote-sensing" analysis of the shape and location of Neptune's bow shock prior to the inbound bow shock crossing. The bow shock is assumed to have a paraboloidal shape with a nose location and flaring parameter determined independently for each wave event. The nose of Neptune's bow shock is found to move monotonically planetwards from $46.5R_N$ to $45.1R_N$ and from $38.5R_N$ to $34.2R_N$ during the two periods of wave activity. The remote-sensing analysis gives a shock position consistent with the time of the inbound shock crossing. The flaring parameter of the shock remains approximately constant throughout

each period of wave activity but differs by a factor of 10 between the two periods. Location of the shock's nose near $46R_N$ during the first wave period is consistent with the observed variations and magnitude of the solar wind ram pressure. The absence of waves between the two periods of wave activity coincides with a large rotation of the magnetic field and a large increase in the solar wind ram pressure; both these effects lead to magnetic disconnection of the spacecraft from the shock. Importantly the planetwards motion of the shock's nose from $38.5R_N$ to $34.5R_N$ during the second time period occurred while the solar wind ram pressure remained constant to within 15%. This second period of planetwards motion of the shock is therefore strong evidence for Neptune's bow shock moving in response to the rotation of Neptune's oblique, tilted magnetic dipole. Normalizing by the ram pressure, the remotely-sensed shock moves sunwards during the first wave period and planetwards in the second wave period. The maximum standoff distance occurs while the dipole's axis is close to being perpendicular to the Sun-Neptune direction. The remote-sensing analysis provides strong evidence that the location of Neptune's bow shock is controlled by Neptune's rotation phase. These data should permit testing of detailed theoretical models for changes in the position and shape of Neptune's bow shock with the phase of Neptune's rotation and solar wind ram pressure variations.

1 Introduction

Electron plasma waves, commonly called Langmuir waves, have provided the first evidence for the existence of a bow shock at each of the outer planets visited by the Voyager spacecraft [Scarf et al., 1979; Gurnett et al., 1981a; Gurnett et al., 1986; Gurnett et al., 1989]. Neptune was no exception. Approximately 4 hours before crossing Neptune's bow shock the plasma wave receiver (PWS instrument) on the Voyager 2 spacecraft first observed waves identified as Langmuir waves [Gurnett et al., 1989]. These waves were then observed intermittently until Voyager passed through Neptune's bow shock near 1445 SCET, 24 August 1989. Subsequent comparison with the ion density measured by the Voyager thermal plasma (PLS) instrument confirmed that these waves had frequencies near the electron plasma frequency, as expected for Langmuir waves.

The standard model for generation of these waves involves electrons accelerated at the quasi-perpendicular regions of the bow shock, near the tangent point, streaming sunwards from the shock along the magnetic field and driving the waves by the ordinary two-stream or bump-on-tail instability [Scarf et al., 1971; Filbert and Kellogg, 1979; Cairns, 1987a,b; Gurnett et al., 1989, and references therein]. Accordingly, the presence of the waves is interpreted in terms of the spacecraft being magnetically connected to a region of the shock near the tangent point which is producing energetic electrons; the spacecraft is said to be located in the planet's electron foreshock [e.g., Klimas, 1984]. If the spacecraft is assumed to be magnetically connected to the tangent point when the electron plasma waves are observed, then the characteristic shape and location of the bow shock can be inferred [e.g., Fuselier et al., 1985]. Thus, by studying variations in the plasma wave and magnetic field data one can perform a "remote-sensing" analysis of the

characteristics of a planet's bow shock. In this paper we use this technique to remotely infer the existence of large-scale changes in the position and shape of Neptune's bow shock prior to Voyager 2's inbound crossing of the bow shock. In different time periods these changes are separately interpreted in terms of rotation of Neptune's tilted magnetic dipole and solar wind ram pressure variations.

Belcher et al. [1989] and Ness et al. [1989] have suggested that the rotation of Neptune's oblique, tilted magnetic field should produce periodic changes in the structure of Neptune's magnetosphere and magnetopause. Theoretical modelling of this situation confirms these periodic changes in magnetospheric structure [Voigt and Ness, 1990]. It is possible that variations in the location and/or shape of the bow shock might accompany these changes in magnetospheric structure. In this paper we present the first experimental evidence that rotational control of Neptune's bow shock, and so the magnetosphere as a whole, does indeed occur. The bow shock positions and shapes derived in this paper will enable testing of future theoretical models attempting to describe time variations in the structure and location of Neptune's bow shock.

The framework of this paper is as follows. Section 2 contains an explanation of the theoretical concepts and procedures used in the remote-sensing analysis. The plasma wave data are presented and discussed in Section 3, after which the magnetic field data are presented in Section 4. Section 5 presents the variations in the position and shape of Neptune's bow shock inferred from the remote-sensing analysis. Voyager 2's trajectory relative to the inferred tangent points and shock locations is described in Section 6. In Section 7 we separate the large-scale motions of the bow shock into motions caused by variations in the solar wind ram pressure and variations caused by rotational changes in the orientation of Neptune's magnetic dipole relative to the solar direction. The results of the paper are discussed in Section 8 and the conclusions

are given in Section 9.

2 The Remote-Sensing Analysis: Theoretical Concepts and Background.

Figure 1 illustrates the amplitude of electron plasma waves expected when a spacecraft enters a planetary foreshock along the trajectory indicated. Energetic electrons streaming away from the shock, and the associated Langmuir waves, are constrained to lie downstream from the magnetic field line tangent to the bow shock. This region is called the electron foreshock [e.g., Klimas, 1984]. Changes in the magnetic field direction and/or the shock shape and location of the bow shock, as well as the spacecraft's motion, can cause the foreshock's streaming electrons and associated Langmuir waves to sweep over the spacecraft, resulting in the appearance and disappearance of the waves.

Neglecting the solar wind speed relative to the electron streaming speed, the spacecraft position and magnetic field direction corresponding to the onset or disappearance of the waves at the upstream edge of the foreshock define the magnetic field line connecting the spacecraft to the tangent point on the bow shock. A natural Neptune-centered coordinate system analogous to the GSE system is used: the X axis points sunwards from the planet, the Y axis lies in the planet's orbital plane, and the Z axis completes a righthanded coordinate system. The equation of a magnetic field line with orientation (B_X, B_Y, B_Z) passing through the spacecraft position (X_{sc}, Y_{sc}, Z_{sc}) is

$$\frac{X - X_{sc}}{B_X} = \frac{Y - Y_{sc}}{B_Y} = \frac{Z - Z_{sc}}{B_Z} = t. \quad (1)$$

The bow shock is represented by the paraboloid

$$X = a_s - b_s(Y^2 + Z^2) \quad (2)$$

where the parameter a_s is the nose position of the shock and the parameter b_s is related to the flaring of the shock. Aberration of the bow shock due to Neptune's orbital motion is of order 0.7° and is neglected here. Choice of a paraboloid shock shape, rather than a hyperboloid for example, is justified by (1) the tangent points found in this paper are all near the nose of the shock where the paraboloidal description is more appropriate, (2) algebraic simplicity, and (3) convention in connection analyses [i.e., Filbert and Kellogg, 1979; Fuselier et al., 1985]. Discussion of the symmetry of the shock surface is deferred to Section 8. The parameter b_s is related to the transverse distance $\rho_T = (Y^2 + Z^2)^{1/2}$ of the shock from the Sun-Neptune line at $X = 0$, i.e. the effective obstacle width, by $\rho_T = \sqrt{a_s/b_s}$.

Constraints on the shock parameters a_s and b_s follow on considering the conditions for magnetic connection of the spacecraft to the tangent point. Equation (1) is rewritten as three separate expressions for X , Y and Z as a function of the t parameter, the magnetic field components and the spacecraft position. A quadratic equation for t is obtained by substituting these expressions into equation (2) and rearranging. Noting that connection of the spacecraft to the tangent point corresponds to this quadratic equation having only one real solution, the constraints on the tangent point follow from the quadratic determinant being zero. This procedure gives two results. First, a relation between the a_s and b_s parameters of the shock in terms of the magnetic field components and spacecraft position:

$$X_{sc} = a_s + \frac{B_X^2}{4b_s\alpha} + \frac{\beta B_X}{\alpha} + \frac{\beta^2 b_s}{\alpha} - \gamma b_s \quad (3)$$

Here $\alpha = B_Y^2 + B_Z^2$, $\beta = B_Y Y_{sc} + B_Z Z_{sc}$ and $\gamma = Y_{sc}^2 + Z_{sc}^2$. Notice that a_s and b_s cannot be

determined uniquely by this procedure from the spacecraft position and magnetic field direction for one foreshock crossing. However, values for a_s and b_s can be determined uniquely if the tangent line is crossed twice (with the shock remaining stationary) by solving the two versions of equation (3) simultaneously. This technique is termed the “conventional analysis” hereafter. Alternatively, best-fit or least-squares techniques can be used in the over-determined case where more than two sets of single point magnetic field vectors and spacecraft locations are identified with crossings of the foreshock boundary. The second result specifies the t parameter, and so the location, of the tangent point:

$$t = -\frac{\frac{Bx}{b_s} + 2\beta}{2\alpha}. \quad (4)$$

Once the parameter b_s is known, the location of the tangent point can be calculated using equations (1) and (4).

In practice the idealized procedure described above may encounter difficulties in adequately identifying the times of foreshock entrances and exits for the remote-sensing analysis. These difficulties include low time resolution data, spacecraft interference signals, instrumental backgrounds significant compared with the wave levels on the most nearly tangent magnetic field lines (e.g., compare Figures 1 and 2), and multiple foreshock encounters in close succession that may not be time-resolvable. Unfortunately, these problems are all relevant to the analysis of the Neptune foreshock data. Two techniques used here to resolve these difficulties involve (1) consideration of peak events in the wave data, and (2) consideration of the entire excursion into and out of the foreshock. Essentially both these techniques involve broadening the definitions of wave events identified with magnetic connection to the tangent point, thereby permitting minimization of interference effects due to time-averaging and rejection of deviant data points.

The two classes of wave data corresponding to these two techniques are denoted by symbols ‘p’ and ‘o’ in Figure 2b and are described in detail in the next Section.

Observational and theoretical justifications for these techniques are now explored. It is well known that the highest Langmuir wave levels are observed near the upstream edge of Earth’s foreshock [Filbert and Kellogg, 1979; Etcheto and Faucheux, 1984; Gurnett, 1985, Figure 11]. Accordingly, the observation of a localized peak in the wave data can be taken as evidence for the spacecraft being very near to the upstream edge of the foreshock. Ideally confirmation of this identification should be possible from the magnetometer data: time variations in the magnetic field data should coincide with the wave peak and be qualitatively suitable for positioning the spacecraft near the upstream boundary of the foreshock. At Neptune we found that essentially all of the peak wave events analyzed had appropriate associated magnetic signatures, thereby justifying our analysis of peak wave events in this paper. Discussion of intrinsic “clumps” in the wave data not related to magnetic field variations is deferred to Section 8. The justifications for our second technique, consideration of complete excursions into and out of the foreshock (the so-called “on/off” events introduced in the next section), rely on the finite spatial width of the foreshock region containing significant wave levels. Observationally, the region of an electron foreshock containing high wave levels is expected to have a finite spatial width, as indeed observed at Earth [e.g., Figure 11, Gurnett, 1985]. Theoretically, as shown in the Appendix, the thickness of the high wave level region of the foreshock is also well-defined: measured from the tangent field line, this region is expected to have a maximum angular width less than 10° at Neptune. Although not ideal, even the worst case scenario when the remote-sensing analysis is performed for a data set comprising the time period of a complete traversal of the high wave region of the foreshock (in effect identifying all times with the tangent field line) should lead only to relatively

small errors in the inferred shock characteristics. In practice, events in which the spacecraft does not move through the entire high wave region of the foreshock can be distinguished qualitatively using the magnetometer data and the amplitude history of the waves. These events comprise locations significantly less than 10° downstream from the tangent field line, thereby reducing the errors introduced by identifying all members of the data set with the tangent field line and increasing our confidence in the results from the remote-sensing analysis. We have favored use of these partial foreshock traversals in our analyses.

Before discussing the wave data we briefly compare these two techniques in terms of closeness to the idealized remote-sensing analysis and sensitivity to interference signals. In comparison to the second technique, in which data from the entire region with higher than background wave levels (nominally $0 - 10^\circ$ from the tangent field line) are identified with the tangent field line, the peaks technique has the stronger observational and theoretical justification. However, due to the smaller number of points analysed in each data set for the peak events, the peak data sets should be more subject to the effects of spacecraft interference signals.

3 Plasma Wave Data

The characteristics of the Voyager plasma wave instrument are described by Scarf and Gurnett [1977]. Here we are concerned only with electric field data from the 16 channel spectrum analyzer system; no wideband frames were taken while Voyager 2 moved through Neptune's foreshock. A complete plasma wave spectrum from 10 Hz to 56.2 kHz is available every 4 seconds. Overviews of the plasma waves detected during the Neptune encounter are given by Gurnett et al. [1989]. Figure 2a shows a 20 second time-averaged history of all the Langmuir

waves observed in Neptune's foreshock. The waves were observed from 1040 - 1440 SCET, day 236, 1989 during the inbound pass. No Langmuir waves have presently been identified in the outbound foreshock data. The figure shows that the Langmuir waves were confined to the 562 Hz channel except for a few spiky events in the 1 kHz and 311 Hz channels. Waves were observed during two periods, 1040 - 1115 SCET and 1240 - 1440 SCET, with an intervening 85-minute period without observable waves. The time period during which Voyager traversed the inbound bow shock according to the plasma wave data, 1435 -1448 SCET, is shown by the two vertical dashed lines (Moses et al. [1990] discuss this time period in detail). The level of Langmuir waves decreases to zero as the spacecraft moves closer to and into the shock and downstream region. During the two observation periods many distinct wave events occur, often with several peaks per event. This is true for both the well-separated wave events observed from 1040 - 1115 SCET and the more continuous wave events from 1240 - 1440 SCET. The timing of the wave events, particularly the peak events, are best identified in Figure 2b, where no time averaging is performed. Some care must be taken in interpreting the data in Figure 2b due to the presence of regular spacecraft interference signals and irregularly occurring thruster firings. The regular interference signals may be separated from both Langmuir wave signals and thruster firings by their periodicity in time, duration and amplitude. For instance, the signals from 1030 - 1039 SCET are all interference signals, whereas the signal at 1040:35 SCET occurs during a periodic null of the interference signals, has a larger amplitude and a different time history, and is consequently either a Langmuir wave signal or a thruster firing. It is therefore generally possible to distinguish Langmuir wave events from regular interference signals without great difficulty. In contrast, although Langmuir wave signals can be separated statistically from thruster firings, this often can not be done in specific cases since detailed timing information for

thruster firings is not available. In the PWS data thruster firings are seen as randomly-timed, impulsive signals that are more intense, and so more observable statistically, at lower frequencies and that sometimes extend into neighbouring channels. Thus, the on/off events defined below will not be confused with thruster firings, while peak events may be. The events in the period 1247 - 1249 SCET are not analyzed further because they appear to extend from the 562 Hz to the 1 kHz channel (thereby being possible telemetry errors or thruster firings) and occur in conjunction with bad magnetic field data. The small number of impulsive signals in the 311 Hz and 1.0 kHz channels for the 1040 - 1115 SCET and 1254 - 1440 SCET periods indicates that most probably only a few thruster firings occurred and produced signals in the 562 Hz channel during these periods. Thus, it is probable that at most a few thruster events are misidentified as peak wave events for the remote-sensing analysis.

The presence of many time-separated events in the Langmuir wave data indicates that Voyager entered and left the foreshock many times, thereby permitting multiple determinations of the shock parameters a_s and b_s over a time period of approximately 4 hours. Correlations of the plasma wave and magnetic field data (next section) do indeed confirm that most events in the wave data are definitely associated with changes in the magnetic field direction, and so the connection geometry of the spacecraft. Discussion of the alternate possibility, that the Langmuir waves naturally occur in well-defined clumps while stably located in the foreshock is discussed in Section 8. We distinguish two classes of wave events for analysis. The first class, termed on/off events and given the symbol 'o', consists of the entire portion of a wave event for which the plasma wave amplitude is above the local background level. The second class, termed peak events and given the symbol 'p', consist of the portions of an event immediately surrounding a peak in the wave amplitude. Peak events generally have much shorter time durations than

on/off events. Examples of both on/off and peak events are shown in Figure 2b. These two classes of events have somewhat different interpretations in terms of position in the foreshock (see Section 2): the on/off events correspond to the entire period of the spacecraft being in the high wave region of the electron foreshock, while the peak events correspond to the spacecraft being close to the upstream edge of the foreshock where the highest levels of Langmuir waves are observed in other planetary foreshocks. Despite these differences, observationally we find that the remote-sensing analysis leads to values for the shock parameters a_s and a_e that are consistent and indistinguishable (within the error bars) for the two classes of events considered.

Krimigis et al. [1989] state that the LECP data do not show clear evidence for upstream enhancements of bow shock-associated energetic electrons and ions. The presence of the Langmuir waves is, however, clear evidence for the existence of an electron foreshock and energetic upstream electrons; the large threshold energy for the LECP's electron detectors (22 keV, corresponding to 200 thermal speeds) is probably the reason for the lack of observed energetic electrons. Given that the Langmuir wave data infer multiple entries into and exits from the electron foreshock, it is natural to inquire whether the plasma wave data show any evidence of entry into an ion foreshock region. Searches for lower frequency electrostatic waves interpretable as ion acoustic waves driven by streaming ions in an ion foreshock, analogous to those observed in the ion foreshocks of Earth [i.e., Anderson et al., 1981; Gurnett, 1985; Thomsen, 1985] and Jupiter [Scarf and Gurnett, 1979], have not met with success to date. Possible reasons for this result are discussed in Section 6.

4 Magnetic Field Data

Behannon et al. [1979] describe the magnetic field instrument on the Voyager-2 spacecraft. The data presented here are 1.92-second averages of the 60-ms vector field measurements from Voyager 2's inboard magnetometer. Data from the outboard magnetometer is unusable at this time due to interference. The inboard magnetometer data has been corrected for spacecraft fields using offsets calculated by R.P. Lepping. For the Neptune encounter the magnetic field data may be transferred from the usual (R, T, N) solar equatorial system to the Neptune-centered system defined in Section 2 by changing the sign of the R and T components: $(B_X, B_Y, B_Z) = (-B_R, -B_T, B_N)$. This procedure should be accurate to within a few percent in each component, corresponding to errors in the magnetic field direction of at most a few degrees.

Figure 3 shows a time series for the magnetic field components B_X , B_Y , and B_Z for the period 1000 - 1400 SCET day 236, 1989, together with the plasma wave data from the 562 Hz channel. The magnetic field is observed to be relatively stable during each half of the four hour period, but exhibits a large rotation that begins at approximately 1115 SCET and ends shortly before 1200 SCET. After this rotation the magnetic field lies almost entirely along the $-Y$ axis. Prior to the rotation the angle in the X-Y plane between the X axis and the magnetic field was approximately -60° , but after the rotation it was approximately -85° as expected on the basis of the Parker spiral model. Similarly, the angle between X axis and the magnetic field in the X-Z plane varied from approximately $+35^\circ$ to -70° before and after the rotation, respectively. Since the spacecraft approached Neptune primarily in the X-Y plane, connection phenomena should be primarily dependent on the angle between the magnetic field and the X axis in the X-Y plane.

Comparing the plasma wave data with the magnetic field data permits one to qualitatively test whether the on/off and peak wave events are associated with changes in the magnetic field direction. Positive changes in the B_X and B_Y components correspond to the magnetic field vector pointing more towards the Sun, and so to sunwards movement of the foreshock. Several wave events that are clearly correlated with changes in the field can be seen in Figure 3. Some wave events are associated with magnetic field changes that are too subtle to be seen on the scale used in Figure 3. Close inspection of these events usually shows that small fluctuations of the magnetic field consistent with a change in magnetic connection do occur at these times. However, as discussed below, the magnetic field data is contaminated with spacecraft interference signals. It appears that these interference signals sometimes disguise the field variations corresponding to a wave event and at other times suggest that a wave event should have occurred where none was observed. In summary, the magnetic field data imply that most wave events are definitely associated with magnetic connection and disconnection from the bow shock.

The large rotation of the field between 1115 and 1200 SCET is clearly a likely cause for the spacecraft being disconnected from the shock surface as evidenced by the lack of plasma waves from 1115 - 1240 SCET. In Section 7 we show that the solar wind ram pressure also increases by a factor of order 3 during this time period, thereby being another cause for disconnection of the spacecraft from the shock. The resumption of wave activity near 1240 SCET with the new field configuration indicates renewed connection to the shock. The absence of additional large rotations of the magnetic field associated with resumption of the wave activity, and the sense in which the one large rotation between 1120 and 1200 SCET occurred, is important, however, in providing the first evidence for large scale motions of Neptune's bow shock. Figure 4 shows this evidence. From the spacecraft positions at times 1115 and 1255 SCET and the corresponding

time-averaged magnetic field directions, we can obtain two equations analogous to equation (3) for a_s and b_s . Solving these equations simultaneously we obtain the values $a = 38.5 R_N$ and $b = 5.66 \times 10^{-3} R_N^{-1}$. The inferred shock surface, the spacecraft trajectory before and after 1255 SCET, and the tangent magnetic field lines at 1115 and 1255 SCET are shown in Figure 4. Assuming that no changes in the shock characteristics occurred, this figure shows that Voyager 2 should have crossed the shock shortly after 1255 SCET. This prediction may only be reconciled with the observed shock position near 1445 SCET if large scale motions of the shock occur.

The analysis of connection events evident in the plasma wave data is complicated by the presence of high levels of interference signals in the magnetic field data. These interference signals are discussed extensively by Russell et al. [1990] for the Uranus encounter. Figure 5 shows the diagonal elements of the spectral density matrix for the magnetic field data from 1000 - 1400 SCET, day 236. These power spectra are very similar to those calculated for a similar data interval 1 week earlier (Day 229, 17 August, 1989). Strong interference is immediately apparent from 3.9 mHz (256 second period) to frequencies greater than 0.1 Hz. These signals correspond to a 768-second pure tone, and its harmonics, associated with operation of the spacecraft. The fundamental pure tone is evident in spectra computed for longer periods of time. The frequency breadth of each harmonic signal in Figure 5, ideally a pure tone, is determined by the smoothing required to provide statistical weight to the physically significant spectral elements. The spectra shown were smoothed over 13 adjacent spectral estimates to provide a statistical weight of 26. The associated 96% confidence level is shown in the figure. All components of the measured magnetic field vector are affected by the interference.

The presence of strong interference signals in the magnetic field data at frequencies up to the sampling rate for the data used here (0.52 Hz) means that individual magnetic field data points

cannot be trusted implicitly. Unfortunately we cannot perform a filtering analysis to remove these interference signals since the connection analysis performed here depends sensitively on the magnetic field direction (and so the phase of the unfiltered signal). The approach adopted here is to minimize the interference using a graphical/least-squares analysis with the two classes of wave events identified in the last section: on/off events and peak events. We identify the entire time period of each event with continual connection to the tangent point, relying on the small angular extent of the foreshock and the other justifications in Section 2. Each such time period has a set of measured (contaminated) magnetic field vectors. Combining this set of vectors with the spacecraft position for the center of the event leads to a set of equations relating a_s and b_s via equation (3). Best fit values of a_s and b_s are obtained using two techniques: a graphical analysis that obtains a best fit to simultaneous solutions of the set of equations and a conventional least squares analysis. We note that the conventional means of calculating a_s and b_s , a simultaneous solution of the two versions of equation (3) corresponding to pairs of upstream entrances to or exits from the foreshock, is a special case of the generalized analysis for an isolated peak event or brief on/off event with only two associated magnetic field data points. Thus, if the different wave events analyzed introduce no systematic differences, the results of the conventional analysis and the more general analyses used here should agree closely once interference effects are removed.

5 Calculated Shock Characteristics

The graphical method for determining the shock parameters a_s and b_s is illustrated for the on/off event from 1044:11 - 1044:51 SCET in Figure 6. The 20 magnetic field vectors for this event are combined with the spacecraft position at 1044:31 SCET to give 20 relations between

a_s and b_s . These 20 relations between a_s and b_s are plotted as the 20 curves in Figure 6. The curves show a well-defined intersection at $a_s = 46.6 \pm 0.2 R_N$ and $b_s = 0.029 \pm 0.001 R_N^{-1}$. These are the best-fit estimates for a_s and b_s resulting from the graphical analysis. We also performed a least squares analysis by minimizing the difference between the left and right hand sides of equation (3) for this set of 20 magnetic field vectors. Unfortunately, the least squares analysis for this event converged to a negative value of b_s and was discarded. Figure 7 shows the graphical analysis for the peak event from 1101:03 - 1101:15 SCET. The best-fit values are $a_s = 45.5 \pm 0.2 R_N$ and $b_s = 0.027 \pm 0.01 R_N^{-1}$. For this event the least squares analysis converged to $a_s = 45.6 R_N$ and $b_s = 0.027 R_N^{-1}$, in excellent agreement with the graphical analysis. Note that this on/off event and the peak event give qualitatively consistent shock parameters. The quantitative differences between these two events are due to motion of the shock, as shown below. Before proceeding, we confirm two essential results. (1) The generalized remote-sensing analyses developed here and the conventional analysis (only data from pairs of entrances/exits of the foreshock) lead to shock parameters that are identical within the error bars once clearly deviant points are excluded. This is true for all events throughout the period 1040 - 1435 SCET for which the analysis techniques have been compared. Thus, no systematic differences in the shock parameters can be distinguished between the generalized remote-sensing analyses developed here and the conventional analysis (corrected for severely interference-affected data). (2) Independent connection analyses show that the remote-sensing analysis does produce shock parameters consistent with the spacecraft being magnetically connected to the bow shock when the wave events occur. We note moreover that the connection analyses demonstrate that even small changes in the shock position and magnetic field direction are sufficient to connect and/or disconnect the spacecraft from the bow shock, consistent with the great time variability in the

observed wave data and the generally small variations in the observed magnetic field direction.

We have analyzed all of the well-defined on/off events and many of the peak events in the plasma wave data using the generalized remote-sensing analysis. The values of the shock nose position a_s inferred from these analyses are shown as a function of time in Figure 8. The time and X position of the shock crossing are also shown. The error bars shown correspond to the graphical analysis. Four important results are visible in the Figure. First, the nose of Neptune's bow shock moved from about $46.5R_N$ to $34.5R_N$ from 1040 to 1430 SCET, Day 236, 1989. These large scale motions correspond to variations of at least 25% in the nose position. Second, Voyager 2 crossed the bow shock at a position $(34.0R_N, 8.3R_N, 0.4R_N)$ consistent with the shock parameters inferred from the remote-sensing analysis. Third, both major periods of wave activity (1040 - 1115 SCET and 1240 - 1430 SCET) show monotonic decreases in the nose position a_s with time, corresponding to planetwards motion of the shock. Fourth, the time variations in nose position for the two periods of wave activity do not lie on the same line or have the same inferred shock speeds (slopes). The inferred shock speeds in the X direction are commensurate with the spacecraft speed.

Figure 9 shows the time variations in the flaring parameter b_s inferred from the remote-sensing analysis. Two important results follow from the figure. First, the flaring parameter b_s varied by a factor of 10, corresponding to a factor close to 3 in the transverse thickness ρ_T , between 1040 and 1435 SCET, Day 236. Second, no evidence for monotonic variations in b_s exists. Instead, the b_s parameter varies discontinuously by a factor of 10 between the two periods of observed wave activity.

Models for Neptune's bow shock, based on the plasma particle and magnetic field data when Voyager-2 crossed the bow shock on the inbound and outbound trajectories, are given by Belcher

et al. [1989] and Ness et al. [1989]. For $X \geq 0$ these authors' hyperboloidal shock shapes are closely approximated by paraboloids. Values for a_s and b_s in these models can be calculated from Figure 2 in each paper. The Belcher et al. model, termed the PLS model here, has $a_s \sim 34.7 R_N$ [M. Zhang, personal communication, 1991] and $b_s \sim 0.010 R_N^{-1}$. The Ness et al. model, termed the MAG model, has $a_s \sim 34.2 R_N$ and $b_s \sim 0.008 R_N^{-1}$. Arrows indicating the parameters for the MAG and PLS models are shown in Figures 8 and 9. The MAG and PLS models therefore have values of a_s that are consistent with the remote-sensing analysis for the inbound shock crossing. However, the remote-sensing analysis gives values of b_s (and so the transverse extent ρ_T of the bow shock) that are very different from those for the MAG and PLS models. Reasons for this difference are explored in Section 6.

6 Shock Shapes and Spacecraft Trajectory

The shape and location of Neptune's bow shock varies significantly with the varying shock parameters shown in Figures 8 and 9. The full lines in Figure 10 show the shock shapes inferred from the remote sensing analysis at times 1045, 1305 and 1440 SCET. Voyager 2's trajectory is shown with open circles spaced by 30 minute time intervals. The two dashed lines show the locations of the MAG and PLS shock models. During the wave events between 1040 and 1115 SCET the shock is inferred to have a very elongated shape, while after 1240 SCET the shock has a very blunt shape with very large transverse extent. The MAG and PLS shock shapes have much smaller transverse thicknesses than the shock shapes inferred after 1240 SCET. However, for $X < 30 R_N$ the MAG and PLS curves lie between the extreme shock shapes found here (the 1045 and 1305 SCET shapes).

Comparison of the shock shapes determined in this paper with the MAG and PLS shock shapes leads to four points. First, Figure 10 indicates that the remotely-sensed 1440 SCET shock and the MAG and PLS models all accurately represent the location of the inbound shock crossing. Second, the variations in remotely-sensed shock shape shown in Figure 10 imply that Neptune's bow shock moves through huge spatial volumes downstream from the planet. This implies the possibility of multiple shock crossings downstream from the planet along the outbound trajectory, as indeed observed [Belcher et al., 1989; Ness et al., 1989]. Third, the values of b_s determined here bracket the values of b_s from the MAG and PLS models, which themselves differ by a factor of 2. It is therefore quite possible that this range in b_s is correct. Lastly, however, the blunt shock shapes characteristic of the time period after 1240 SCET cannot predict the observed locations [Belcher et al., 1989; Ness et al., 1989] of the outbound bow shock crossings. The outbound bow shock crossings are observed in the ranges $-126R_N < X < -110R_N$ and $115R_N < \rho = \sqrt{Y^2 + Z^2} < 135R_N$; for this range of X the blunt shock shapes in Figure 10 have $220R_N < \rho < 235R_N$, while the elongated shock shapes have $\rho \sim 70R_N$. A natural resolution of this discrepancy is that the values of b_s determined using the remote-sensing analysis are local values appropriate to the nose of the shock but not to the shock as a whole. In addition, part of this discrepancy may be due to the paraboloidal (and not hyperboloidal) shape assumed for the shock in the remote-sensing analysis. This matter is discussed further in Section 8.

The position of the tangent point on the shock for each connection event, and the position of the spacecraft relative to the tangent point, may be estimated using the analysis in Section 2: connection of the spacecraft to the tangent point at a particular time gives a value for the t parameter and so the position (X_t, Y_t, Z_t) for the tangent point. Figure 11 compares the average X , Y and Z positions of the tangent point for each connection event with the spacecraft trajectory.

This figure shows that the spacecraft always remains within about $0.5R_N$ of the tangent point in the X and Z directions, while always lying within $10R_N$ (and usually within $3R_N$) of the tangent point in the Y direction. These numbers are consistent with the nominal 10° width of the electron foreshock derived in the Appendix: within a distance of $3R_N$ along the magnetic field (or Y direction) from the tangent point the electron foreshock should extend less than about $0.5R_N$ downstream in the X direction. The tangent points are calculated to lie at values of X, Y and Z that are sometimes larger and sometimes smaller than the spacecraft coordinates, corresponding to the tangent point moving from one side to the other of the spacecraft trajectory. The spacecraft was therefore in the upstream wing of the foreshock (e.g., Figure 1) for some connection events and in the downstream wing for others. This behaviour, and the clustering of the coordinates of the tangent points around the spacecraft trajectory, indicates that variations in the magnetic field and shock characteristics led to the inbound Voyager trajectory almost continuously following the tangent point planetwards.

The multiple on/off events in the plasma wave data (Figures 2a,b) have a natural explanation in terms of the observed magnetic field variations causing the tangent point to flicker from one side of the spacecraft to the other (along the magnetic field direction) with associated onsets and absences of the shock-accelerated electrons. In the absence of magnetic field variations the observed on/off events would have to be explained in terms of time variations in the energetic electrons or natural clumping of the waves while stably connected; no such appeal is necessary here. Planetwards motion of the shock from positions initially near $45R_N$ is necessary to explain the long time duration and range of spatial positions of the foreshock passage for the tightly-wound, relatively constant, and approximately Parker spiral magnetic fields observed during Voyager's nearly nose-on inbound trajectory. Steady rotation of the magnetic field, which might

otherwise permit longer foreshock encounters for a stationary shock, is explicitly ruled out by the magnetic field data. Figures 4 and 10 explicitly demonstrate the brief time duration and small spatial volume in which the spacecraft could encounter the foreshock for the observed magnetic field directions if the shock were stationary. These points are used below to argue that the remotely-sensed variations in a_s shown in Figure 8 must correspond to actual motions of the shock and not to the effects of changes in the orientation and shape of the shock.

The finding that the spacecraft always remains close to the tangent point and the quasi-perpendicular region of the bow shock provides a qualitative explanation for the absence of significant energetic foreshock ions [Krimigis et al., 1989] and associated plasma waves upstream from Neptune. At Earth these ions are observed to be associated primarily with magnetic connection to the quasi-parallel regions of the shock [e.g., Thomsen, 1985]. Qualitatively, therefore, Voyager's inbound trajectory is not suited for observing such foreshock ions and associated plasma waves.

7 Ram Pressure Effects Versus Dipole Orientation Effects

It is well known that variations in the Alfvén Mach number and the ram pressure of the solar wind may compress a planet's magnetosphere and cause large scale variations in the location and shape of planetary bow shocks [e.g., Spreiter et al., 1966; Binsack and Vasyliunas, 1968; Formisano, 1979]. Balancing the solar wind ram pressure with the planet's magnetostatic pressure, the nose position a_s of a bow shock in a high Mach number flow is expected to vary according to [e.g., Spreiter et al., 1966; Binsack and Vasyliunas, 1968; Formisano, 1979]

$$a_s \propto (n_{sw} v_{sw}^2)^{-1/6} \quad (5)$$

where n_{sw} and v_{sw} are the solar wind number density and speed, respectively. Inclusion of both Mach number and ram pressure effects leads to [Spreiter et al., 1966]

$$a_s \propto \frac{M^2 + 3}{4M^2} (n_{sw} v_{sw}^2)^{-1/6} \quad (6)$$

where M is the Alfvén Mach number and the ratio of specific heats is taken to be 5/3. Thus, the bow shock is moved further planetwards by higher Mach number and/or higher ram pressure solar wind flows. The above formulae need further modifications when the planet's magnetic dipole is oriented approximately pole-on to the solar wind flow [e.g., Biernat et al., 1981; Ip and Voigt, 1985]. However, during the period 1000 - 1430 of interest here Neptune's dipole had an approximately Earth-like interaction with the solar wind [see Figure 5, Ness et al., 1989].

Solar wind density, velocity and ram pressure data are available from the Voyager 2 plasma instrument, the PLS instrument [Bridge et al., 1977]. Figure 12 compares the time variations in the solar wind ram pressure given by the PLS instrument (in massless units, $n_{sw} v_{sw}^2$) for the period 1000 - 1500 with the variations in nose position a_s given by the remote-sensing analysis. Ram pressure data are shown at two time resolutions; the open circles show L mode ion data with a 48 second time resolution, while the filled triangles show M mode ion data with a 12 minute time resolution. During this time period the solar wind speed remained constant to within less than 5%; the variations in ram pressure correspond almost entirely to variations in the number density of the solar wind. Only small changes in (Alfvén) Mach number occur due to the solar wind magnetic field increasing with the plasma density (compare Figures 3 and 12): the Mach number increases from 3.5 ± 0.5 near 1000 to an approximately constant value of 4.3 ± 0.7 between about 1200 and the shock crossing. Accordingly, we find below that ram pressure variations are dominant in determining the position of the shock.

The solar wind ram pressure increases by a factor of approximately 3.2 from 1040 to 1200 and remains approximately constant (within about 15%) from 1200 to 1500. According to equations (5) and (6) the bow shock should move closer to the planet as the solar wind ram pressure and Mach number increase and should remain stationary when the ram pressure and Mach number are constant. The remote-sensing analysis infers large-scale, monotonic, planetwards motions of the bow shock during both periods of Langmuir wave activity, 1040 - 1120 and 1240 - 1440. However, the 1240 - 1440 period of inferred planetwards motion occurs while the ram pressure and Mach number are observed to be effectively constant. Thus, Figure 12 provides a first demonstration that the remotely-sensed, monotonic, planetwards motion of the Neptune's bow shock from 1240 - 1440 can not be due to variations in the solar wind ram pressure or Mach number. Instead, an explanation in terms of rotation of Neptune's offset, tilted magnetic dipole is pursued in the next section.

Variations in the solar wind ram pressure (and Mach number) can, however, qualitatively and quantitatively explain most aspects of the inferred shock locations and motions during the period from 1040 - 1120. Qualitatively, the low values and monotonic increase of the ram pressure from 1040 - 1120 (as well as the accompanying minor increase in Mach number) imply that the shock should be moving monotonically planetwards from a location unusually far upstream from the planet, exactly as inferred from the remote-sensing analysis. These ram pressure variations, in conjunction with the magnetic field rotations in Figure 3, then naturally explain Voyager's magnetic disconnection from the shock from 1115 until after 1200. Quantitative comparisons between the remotely-sensed nose positions of the bow shock and the predictions of equation (6) with the observed ram pressure and mach number variations are given in Figure 13. The dot and triangle symbols in the figure show the theoretical ratio $a_{th}(t)/a_0$ predicted by equation (6) using

the L and M mode PLS data, respectively. Here a_0 is the average nose position corresponding to the period 1200 - 1440 of approximately constant ram pressure and Mach number. The remotely-sensed shock nose position a_s , normalized by $38.2R_N$ is shown by the black circles with error bars; this normalization corresponds to the remotely-sensed value of a_s near 1300 when the ram pressure first reaches the steady level corresponding to the a_0 parameter and Langmuir waves are observed. Figure 13 shows three important quantitative results. First, Figure 13 shows that equation (6) and the observed variations in ram pressure and Mach number are quantitatively consistent with the bow shock having $a_s \sim 45R_N$ for much of the period 1040 - 1115 as found using the remote-sensing analysis. For instance, the factor of 3.2 decrease in ram pressure corresponds to a factor of 1.2 increase in a_s , leading to a shock with $a_s = 38.0R_N$ under nominal solar wind conditions expanding to $a_s = 46.1R_N$. Second, the quantitative agreement between these two independent analyses in locating the bow shock's nose near $45R_N$ for the period 1040 - 1115 is a strong argument that the remote-sensing analysis is working correctly. Third, Figure 13 explicitly shows that the monotonic decrease in the remotely-sensed a_s parameter after 1240 can not be understood in terms of variations in the solar wind ram pressure or Mach number. Before proceeding we note that there is one potential difficulty for the above simple interpretation in terms of ram pressure variations: Figure 13 shows that the remotely-sensed values of a_s have a slower time-rate-of-change than that predicted on the basis of equation (6). In the next section this apparent quantitative difficulty is discussed in terms of sunwards expansion of the "base" bow shock associated with Neptune's rotation phase.

8 Discussion

In the previous section we showed that variations in the solar wind ram pressure and Alfvén Mach number can not explain the monotonic, $4R_N$ decrease in the inferred nose position of Neptune’s bow shock from 1240 - 1440 SCET, day 236, 1989. Similarly, surface waves on and flapping of the bow shock can not explain the monotonic nature and long time duration of the inferred planetwards motion. The only natural interpretation for these variations in the shock’s a_s parameter is in terms of changes in the location and/or shape of Neptune’s bow shock due to rotation of Neptune’s offset, tilted dipole magnetic field. Belcher et al. [1989], Ness et al. [1989] and Voigt and Ness [1990] have shown that Neptune’s magnetosphere changes from a “pole-on” to “Earth-like” configuration with Neptune’s rotation phase. Variations in the location and/or shape of the magnetospheric boundaries with rotation phase, such as the bow shock, should be expected to accompany these variations in magnetospheric structure. We believe that the remote-sensing observations from the period 1240 - 1440 provide the first observational evidence that the rotation phase of Neptune’s magnetic dipole controls the location and/or shape of Neptune’s bow shock.

Before proceeding, it is important to realize that the analysis techniques used so far in this paper can not necessarily distinguish between purely planetwards motion of the shock and changes in the shock’s shape and orientation that mimic planetwards motion of the shock. However, there are three strong arguments that the changes in a_s given by the remote-sensing analysis must indeed be predominantly associated with motions of the shock. (1) If Neptune’s bow shock was stably located near where the inbound crossing occurred, the observed magnetic field directions do not permit the spacecraft to enter the foreshock and observe Langmuir waves

until approximately 1430 at earliest (see Figure 10). This is inconsistent with the observed plasma wave data. (2) Given the observed magnetic field directions and spacecraft trajectory, the long time period during which waves were observed upstream of the shock can only be explained by a shock moving continually planetwards. Figures 4 and 10 explicitly demonstrate the small time period which a foreshock/shock crossing should take for a stationary shock with parameters in the physical range spanned by the remote-sensing results and the PLS and MAG models. (3) Combining the conventional theoretical model [Spreiter et al., 1966] for shock wave dependence on ram pressure and Mach number variations with the observed variations in the PLS data leads to a very good qualitative and quantitative explanation for the relative locations of the remotely-sensed shock between the first wave period and the start of the second wave period. This argues that the remote-sensing analysis is properly modelling a moving bow shock. We therefore adopt the simplest interpretation, that the remotely-sensed variations in a_s correspond entirely to planetwards motion of the shock. The possibility that changes in the shock's shape and orientation partially mimic planetwards motion of the shock is discussed below.

Ram pressure and Mach number variations are important in producing the inferred planetwards motion of the bow shock from 1040 until 1115 SCET, but not for the time period 1240 - 1440 SCET. Shock motions due to ram pressure or Mach number variations are now removed, based on conventional shock theory and the PLS data, using equation (6) and the calculations illustrated in Figure 13. The term “base” shock refers below to the shock position and shape normalized to a constant ram pressure and Mach number. The bottom panel in Figure 14 displays the calculated variations in the “base” nose location a_c for both wave periods. Figure 14 clearly shows that the “base” shock moves sunwards during the first wave period and planetwards for almost all the second wave period, with a peak value of a_c inferred during the period

1100 - 1230 SCET. The “base” shock moves at least $5R_N$ planetwards from its peak during the observation period. As anticipated in the last section, the sunwards motion of the “base” shock during the first wave period is consistent with the remotely-sensed a_c values decreasing more slowly than expected on the basis of the solar wind variations (Figure 13). Comparisons between the variations in a_c and the rotation phase of Neptune’s dipole are also possible using Figure 14. The figure’s top panel gives the (Neptunian) magnetic latitude and longitude of the Sun as a function of time. The dipole is exactly perpendicular to the solar wind direction when the Sun’s magnetic latitude is zero (near 1402 SCET) and is most “pole-on” to the solar wind when the Sun’s magnetic latitude is -69.9° near 1907 SCET [see also Ness et al., 1989]. Defining the solar wind-dipole interaction to be “Earth-like” when the dipole is within 20° of being perpendicular to the solar wind direction interaction, the peak in a_c definitely occurs in the “Earth-like” period. In more detail, the peak in a_c occurs between the times of the Sun having its peak positive magnetic latitude with zero magnetic longitude (1105 SCET) and the time of zero magnetic latitude (perpendicular dipole) with a magnetic longitude of 57° (1402 SCET).

A simple intuitive model for rotational control of the location of Neptune’s bow shock is the following “compressibility” model. (1) When Neptune’s magnetic dipole is approximately parallel to the Sun-Neptune line (“pole-on” magnetosphere), the magnetosphere should be least able to resist compression by the solar wind, leading to a relatively small standoff distance. (2) The magnetosphere should be less compressible during the Earth-like configuration, thereby implying larger standoff distances for the shock. The peak and subsequent monotonic decrease in a_c (after 1300) during the Earth-like period in Figure 14 are both therefore qualitatively consistent with the compressibility model. Nevertheless, a detailed theoretical understanding of

the data in Figure 14 is not currently available in terms of published theoretical models [e.g., Olsen, 1969; Ip and Voigt, 1985; Voigt and Ness, 1990, and references therein]. For instance, while Voigt's calculations [personal communications, 1990, 1991] show that Neptune's subsolar magnetopause distance should vary by a factor of 2 with rotational phase, with a minimum when the dipole is most nearly pole-on, these changes correspond primarily to the indentation of the polar cusp while the overall size of the magnetopause remains effectively constant (see Voigt and Ness' [1990] Figure 1). Similarly, Olsen [1969] finds that changing the dipole tilt angle by 30° from the perpendicular solar wind-dipole case, corresponding to the period 1040 - 1430 SCET considered here, leads to changes in magnetopause position of only a few percent. Further research is necessary to resolve these questions and lead to a detailed understanding of Figure 14. It is worthwhile pointing out several potentially important limitations of the available theoretical models for bow shock/magnetosphere structure and size. The first limitation is that most theoretical models only explicitly address the structure and location of the magnetopause; little theoretical effort has been devoted to the bow shock itself. Second, the magnetopause size and shape is determined using non-self-consistent analyses that usually neglect the solar wind magnetic field, the plasma flow and magnetic field in the magnetosheath, magnetic flux entry into the magnetosphere (i.e., magnetic reconnection), and often the magnetospheric plasma itself. Third, the effects of time variations in the dipole's orientation, rotationally-induced magnetic field components, and time-varying Alfvén wave stresses are neglected in discussing both the magnetopause and the bow shock. There is therefore considerable scope for theoretical efforts intended to explain the results in Figure 14 and the remainder of this paper.

Arguments against changes in only the shape and orientation (and not standoff distance) of the shock mimicking the remotely-sensed variations in a_s and b_s are given above. Nevertheless,

Neptune's rotation might be expected to cause important modifications of the shape of Neptune's bow shock. For instance, both Jupiter and Venus are known to have bow shocks with asymmetric shapes and variability. In particular, Jupiter's bow shock/magnetopause system is asymmetric and undergoes oscillations at Jupiter's rotation period [Engle and Beard, 1980; Lepping et al., 1981; Smith and Lee, 1986], while Venus' asymmetric bow shock changes its location with the solar cycle [Russell et al., 1988; Zhang et al., 1990]. Changes in the location of the dipole and the compressibility of the sub-solar magnetosphere with Neptune's rotation phase may lead to an asymmetric shock shape. Determination of the asymmetric characteristics of Neptune's bow shock via the remote-sensing technique requires magnetic connection of the spacecraft to many widely-separated parts of the shock. Figure 11 indicates that the spacecraft was most likely connected too close to the shock's nose for such an analysis to be successful. Nevertheless, we generalized the constraint (3) so as to permit the symmetry axis of the shock, as well as the a_s and b_s parameters, to be determined using a least-squares technique. The symmetry axis of the shock was defined in terms of the angles α and β relative to the X axis in the $X - Y$ and $X - Z$ planes, respectively. The analyses performed to date indicate that the preferred solutions to the shock shape and location involve the symmetry axis being aligned with the X axis, thereby supporting the analyses performed in Sections 5 and 6. Nevertheless, if future theoretical modelling suggests that a particular asymmetric shape is appropriate for Neptune's bow shock, it should be a simple matter to adapt the remote-sensing technique used here to test the theoretical shock shape.

Voyager's speed is commensurate with the planetwards speed of the shock. Thus, presuming that the shock continued to move planetwards after the inbound bow shock crossing, consistent with the discussion above, it is likely that the actual thicknesses of the shock layer, the magne-

tosheath and the magnetopause are substantially smaller than those inferred directly from timing measurements. Similarly, given the rotational control of Neptune’s magnetosphere demonstrated above, particular care must be given to properly separating time and spatial variations in the plasma and magnetic field data.

In Section 5 we showed that the flaring parameters b_s , given by the remote-sensing analysis cannot immediately explain the locations of the observed outbound shock crossings. In particular, the shock shapes found prior to 1115 and after 1240 predict that the shocks should be at transverse distances of order $70R_N$ and $230R_N$, respectively, for the observed X locations of the outbound bow shocks; in contrast, the observed transverse distances were of order $130R_N$. While part of this discrepancy may be due to the shock being globally best represented as a hyperboloid rather than a paraboloid, the most likely explanation is that the remote-sensing analysis determines values of b_s appropriate to the shock nose rather than global values appropriate to the shock as a whole. This may be seen as follows. Taking the magnetic field data in Figure 3 and the shock shapes in Figure 10 it is easy to see that Voyager is always located relatively close to the nose of the shock, and indeed to the tangent point. This is particularly true for the shock shapes determined after 1240; in this case the curvature of the shock is also extremely small. Figure 11 explicitly shows that the spacecraft is always close to the tangent point on a global scale. Similarly, the lack of magnetic field variations suitable for connecting the spacecraft to portions of the shock far from the nose restricts our information on the global characteristics of the shock. In summary, our analyses apply solely to the immediate vicinity of the shock’s nose. In this case, the shock could locally (i.e., near the nose) be shaped as determined by the remote-sensing analysis but have a global value of b_s similar to those for the MAG and PLS models. This would naturally permit the shock to be located where observed during

the outbound shock crossings. Theoretical modelling of variations in the shape of the bow shock in response to Neptune's rotation and ram pressure variations should provide a definitive test of this suggestion in the future.

Intrinsic time variations in wave levels while stably connected in the foreshock, corresponding to well-defined wavepackets for example, could conceivably be misidentified as connection/disconnection events with resulting implications for the remote-sensing analysis. Detailed wideband observations at Jupiter show Langmuir waves occurring in well-defined wavepackets with intrinsic time variability on timescales of order 10 ms and below [Gurnett et al., 1981b]. At Earth, while well-defined wavepackets near the plasma frequency have not been distinguished in the data, the waves often show time variations on scales of order 30 ms [Anderson et al., 1981; Etcheto and Faucheux, 1984; Fuselier et al., 1985; Lacombe et al., 1985]. It is therefore likely that the Langmuir waves in Neptune's foreshock do, at least sometimes, occur in well-defined wavepackets with timescales of order a few hundred milliseconds or less. The question here is the sensitivity of the 16 channel spectrum analyzer data used in this paper (Figure 2) to these wavepackets. The receiver reports the average logarithm of the electric field in each channel with a 70-ms averaging time constant; the signal is sampled every 4 seconds. When wavepackets have comparable amplitudes and are not well-separated in time the detector is expected to accurately report the average electric field in the plasma. Only when the wavepackets have very different amplitudes and are well-separated in time is the detector expected to show great variability between successive data points or to greatly underestimate the electric fields present in the plasma. The on/off events analysed in the remote-sensing analysis last for more than two data samples and correspond to an entire period with wave amplitudes greater than the background level. On/off events are therefore not subject to confusion with the effects of finite, time-variable

wavepackets. However, wavepacket effects are able to produce occasional isolated peaks in the wave data potentially similar to the “peak” wave events analyzed in the remote-sensing analysis and interpreted there in terms of magnetic connection/disconnection events. This favors the use of on/off events over peak events in the remote-sensing analysis; additional reasons are given in Sections 2 and 3. There are two practical arguments that the on/off and peak events used in the remote-sensing analysis do not suffer significant contamination from wavepacket effects. First, the on/off and peak wave events almost invariably have associated magnetic field variations qualitatively suitable for moving the foreshock over the spacecraft. Second, the lack of scatter in Figures 8 and 9 indicates that few wave events with unrelated magnetic field variations have been included in the analysis. Finally, we note that the results presented in Figures 8 to 14 are primarily based on the analysis of on/off events, particularly for the period 1300 - 1430 SCET. We therefore conclude that the results of the remote-sensing analyses performed in this paper do not suffer from the effects of misidentifying finite wavepacket events in terms of magnetic connection/disconnection events.

9 Conclusions

In this paper we have performed a remote-sensing analysis for the location and shape of Neptune’s bow shock prior to the inbound bow shock crossing. The analysis uses the magnetic fields and spacecraft positions at the times of specific events in the wave data to fit the bow shock shape to a paraboloid with nose position a_s and flaring parameter b_s . Confirmation that the remote-sensing analysis is correctly determining the characteristics of the shock is provided by: (1) the location of the inbound shock crossing is consistent with the results of the remote-sensing

analysis, (2) variations in the shock position are qualitatively and quantitatively consistent with the independently observed variations in the solar wind ram pressure for the first period of wave activity, and (3) independent connection analyses indicate that the spacecraft locations and magnetic field variations when wave events are observed are consistent with the spacecraft being magnetically connected to/disconnected from a bow shock with the remotely-sensed characteristics. The long time duration, range of spacecraft positions, and number of foreshock encounters during which the Voyager spacecraft observed Langmuir waves along its inbound trajectory require that large-scale motions of Neptune's bow shock occur. The observed ram pressure and Mach number variations are quantitatively consistent with the relative shock positions inferred from the remote-sensing analysis at the start of the two wave periods. Changes in shock shape and orientation can not mimic the inferred shock motions.

The results of the remote-sensing analysis are: (1) Large-scale motions of the bow shock occur while the spacecraft is upstream from the inbound bow shock. In detail, the nose of the bow shock moves from $46.5R_N$ to $34.3R_N$. (2) The nose of the bow shock moves monotonically planetwards during both periods of wave activity (1040 - 1115 and 1240 - 1430). (3) The magnitude and trend in the remotely-inferred nose positions just prior to the inbound shock crossing are consistent with the location of the inbound bow shock. (4) The inferred shock speed is commensurate with (although smaller than) the spacecraft speed. (5) The flaring parameter b_s of the shock remained approximately constant during each period of wave activity, but differed by a factor close to 10 between periods. (6) The remotely-sensed values of b_s bracket those for the MAG and PLS shock models based on the locations of the outbound bow shock crossings. However, these values for b_s are not consistent with the locations of the outbound bow shocks. (7) According to the remote-sensing analysis Voyager was only magnetically connected

near to the shock's nose, thereby only determining values of b_s local to the nose. Discrepancies between the observed outbound shock locations and predictions using remotely-sensed values of b_s are interpreted in terms of global values of b_s being different from values of b_s appropriate to the shock's nose. (8) The location of the bow shock near $45R_N$, and its trend for planetwards motion, during the first period of wave activity are qualitatively and quantitatively consistent with the observed low, but increasing, solar wind ram pressure observed at these times. (9) The remotely-sensed monotonic, planetwards motion of the shock during the second period of wave activity occurs while the solar wind ram pressure and Mach number was constant. With ram pressure-induced motions ruled out, this shock motion is interpreted in terms of the shock location being controlled by the rotation phase of Neptune's oblique, tilted magnetic dipole. (10) Normalizing by the solar wind ram pressure and Mach number according to the conventional Spreiter et al. [1966] formula, the nose of "base" shock is found to move sunwards during the period 1040 - 1115 SCET and planetwards from 1240 - 1430 SCET, with a maximum being inferred in the period 1100 - 1230 SCET.

The maximum standoff distance of the "base" shock occurs during the period 1115 - 1230 SCET while Neptune's magnetic dipole was close to being perpendicular to the solar wind flow. This behaviour is qualitatively consistent with a "compressibility" model in which the shock has a maximum standoff distance when the dipole's rotation phase corresponds to an Earth-like planet-solar wind interaction. A "pole-on" interaction then has a minimum standoff distance. However, no theoretical explanation for these motions of the "base" shock, nor a mathematical basis for the "compressibility" model, is currently available. We conclude that our analyses have experimentally demonstrated that rotational control of Neptune's bow shock/magnetosphere system occurs. This rotational control of the bow shock location (and so perhaps the magnetopause's

location), with the inferred planetwards motion of the shock system (at speeds commensurate with Voyager's speed) after the shock crossing, implies that investigations of Neptune's magnetosheath and magnetopause must take great care to resolve time and spatial variations in plasma and field characteristics. The above results will provide suitable tests for detailed theoretical models for the bow shock/magnetosphere system formed by Neptune's interaction with the solar wind.

The foregoing results have demonstrated the power and utility of remote-sensing techniques using Langmuir waves for detailed investigations of the location and motions of planetary bow shocks. Methods of adapting these techniques for situations with interference-contaminated data have been developed and used successfully here. As should be expected, however, suitable plasma wave, magnetic field and spacecraft location data must be available for a successful and complete analysis to be possible. For instance, the development of global shock models requires magnetic connection of the spacecraft to globally-separated regions of the shock. In the future we hope to use these remote-sensing techniques to investigate other planetary bow shocks.

Acknowledgements

We thank Norman Ness of the Bartol Research Institute and Ron Lepping of NASA's Goddard Space Flight Center for providing the magnetic field data used in this investigation. We thank Ming Zhang and John Belcher of the Massachusetts Institute of Technology for analyzing and providing us with the PLS data shown in Figure 12. IHC gratefully acknowledges the frequent help and computer expertise of Larry Granroth at the University of Iowa. IHC and CWS gratefully acknowledge receipt of unpublished material from and conversations with Hannes Voigt of Rice University. The authors acknowledge financial support from: NASA grant NAGW-

2040 with NASA Headquarters and NASA contract 957723 with JPL at the University of Iowa, NASA contract 957921 with JPL at the Bartol Research Institute, and NASA contract 957805 at TRW.

Appendix: Theoretical structure of the electron foreshock

In this Appendix we describe the theoretical structure of the foreshock with a view to explaining the expected finite width of the region of the foreshock containing high levels of Langmuir waves. As discussed by Filbert and Kellogg [1979] and Cairns [1987a,b], the beam speed of the streaming electrons is a function of position in the foreshock. The streaming electrons move under the influence of the solar wind magnetic field and the solar wind convection electric field \underline{E} . These fields result in a gyrocenter velocity composed of the electron velocity parallel to the magnetic field and an $\underline{E} \times \underline{B}$ drift velocity perpendicular to the magnetic field. This drift velocity always has a component directed in the anti-sunwards, or shockwards, direction. Accordingly, electrons leaving each point on the shock must have a minimum parallel velocity, the so-called cutoff velocity v_c (which varies with position), for the electrons to escape upstream from the local shock surface. These cutoff speeds map into the foreshock along the particle characteristics and lead to the foreshock distribution functions having an abrupt cutoff at the local cutoff velocity v_c : shock-accelerated electrons at the observation position must have $v_{\parallel} > v_c$. Growth of Langmuir waves tends to smooth out the cutoff distribution, leading to a more conventional beam feature with $v_b \sim v_c$. Defining an angle θ between the tangent magnetic field line and the line joining the observation position to the tangent point, one finds that the beam speed is given approximately by

$$v_b = \frac{v_{sw} \sin \theta_{vB}}{\tan \theta} \quad (7)$$

Here θ_{vB} is the angle between the magnetic field and the solar wind velocity v_{sw} defined by $\underline{v}_{sw} \cdot \underline{B} = v_{sw} B \cos \theta_{vB}$. The beam instability is only expected to produce strong levels of waves when the beam speed exceeds about, say, five electron thermal speeds V_e : $v_b > 5V_e$. During

Voyager 2's passages through Neptune's foreshock the PLS data give $v_{sw} \sim 400 \text{ kms}^{-1}$ and $V_e \sim 420 \text{ kms}^{-1}$ assuming $T_e = 2T_i \sim 1\text{eV}$. (The PLS instrument was unable to measure the electron number density and temperature directly in the upstream solar wind.) Then, one finds that the maximum expected width of Neptune's electron foreshock, measured from the tangent field line, is less than 10° . A qualitative summary of this result is as follows: the finite width of the high wave region of the foreshock is due to (1) the beam speed of the streaming electrons being a function of position in the foreshock [e.g, Filbert and Kellogg, 1979; Cairns, 1987a,b] and (2) beam speeds greater than about 5 background electron thermal speeds being required for substantial wave growth.

References.

Belcher, J.W., H.S. Bridge, F. Bagenal, B. Coppi, O. Divers, A. Eviator, G.S. Gordon, Jr., A.J. Lazarus, R.L. McNutt, Jr., K.W. Ogilvie, J.D. Richardson, G.L Siscoe, E.C. Sittler, Jr., J.T. Steinberg, J.D. Sullivan, A. Szabo, L. Villaneuva, V.M. Vasyliunas, M. Zhang, Plasma observations near Neptune: Initial results from Voyager 2, Science, 246, 1478, 1989.

Biernat, H., N. Komle, and H. Rucker, Analytical two-dimensional model for a pole-on magnetosphere, Planet. Space. Sci., 29, 1101, 1981.

Bridge, H.S., J.W. Belcher, R.J. Butler, A.J. Lazarus, A.M. Mauretic, J.D. Sullivan, G.L Siscoe, and V.M. Vasyliunas, The plasma experiment on the 1977 Voyager mission, Space Sci. Rev., 21, 259, 1977.

Cairns, I.H., The electron distribution function upstream from the Earth's bow shock, J. Geophys. Res., 92, 2315, 1987a.

Cairns, I.H., A theory for the Langmuir waves observed upstream from the Earth's bow shock, J. Geophys. Res., 92, 2329, 1987b.

Etcheto, J., and M. Faucheux, Detailed study of electron plasma waves upstream of the Earth's bow shock, J. Geophys. Res., 89, 6631, 1984.

Filbert, P.C., and P.J. Kellogg, Electrostatic noise at the plasma frequency beyond the Earth's bow shock, J. Geophys. Res., 84, 1369, 1979.

Fuselier, S.A., D.A. Gurnett, and R.J. Fitzenreiter, The downshift of electron plasma oscillations in the electron foreshock region, J. Geophys. Res., 90, 3935, 1985.

Fuselier, S.A., W.C. Feldman, S.J. Bame, E.J. Smith, and F.L. Scarf, Heat flux observations and the location of the transition region boundary of Giacobini-Zinner, Geophys. Res. Lett., 13, 247, 1986.

Gurnett, D.A., Plasma waves and instabilities, in Collisionless Shocks in the Heliosphere: Reviews of Current Research, Ed. B.T. Tsurutani and R.G. Stone, AGU, p. 207, 1985.

Gurnett, D.A., W.S. Kurth, and F.L. Scarf, Plasma waves near Saturn: Initial results from Voyager 1, Science, 212, 235, 1981a.

Gurnett, D.A., J.E. Maggs, D.L. Gallagher, W.S. Kurth, and F.L. Scarf, Parametric interaction and spatial collapse of beam-driven Langmuir waves in the solar wind, J. Geophys. Res., 86, 8833, 1981b.

Gurnett, D.A., W.S. Kurth, F.L. Scarf, and R.L. Poynter, First plasma wave observations near Uranus, Science, 233, 106, 1986.

Gurnett, D.A., W.S. Kurth, R.L. Poynter, L.J. Granroth, I.H. Cairns, W.M. Macek, S.L. Moses, F.V. Coriniti, C.F. Kennel, D.D. Barbosa, First plasma wave observations at Neptune, Science, 246, 1494, 1989.

Klimas, A.J., The electron foreshock, in Collisionless Shocks in the Heliosphere: Reviews of Current Research, Ed. B.T. Tsurutani and R.G. Stone, AGU, p. 237, 1985.

Krimigis, S.M., T.P. Armstrong, W.I. Axford, C.O. Bostrom, A.F. Cheng, G. Gloekler, D.C.

- Hamilton, E.P. Keath, L.J. Lanzerotti, B.H. Mauk, J.A. Van Allen, Hot plasma and energetic particles in Neptune's magnetosphere, Science, 246, 1483, 1989.
- Lacombe, C., A. Mangeney, C.C. Harvey, and J.D. Scudder, Electron plasma waves upstream of the Earth's bow shock, J. Geophys. Res., 90, 73, 1985.
- Lepping, R.P, L.F. Burlaga, L.W. Klein, J.M. Jessen, and C.C. Goodrich, Observations of the magnetic field and plasma flow in Jupiter's magnetosheath, J. Geophys. Res., 86, 8141, 1981.
- Moses, S.L., F.V. Coriniti, C.F. Kennel, W.S. Kurth, and D.A. Gurnett, Comparison of plasma waves measured in the bow shocks at Earth, Jupiter, Saturn, Uranus, and Neptune, Geophys. Res. Lett., 17, 1653, 1990.
- Ness, N.F., M.H. Acuna, L.F. Burlaga, J.E.P. Connerney, R.P. Lepping, and F.N. Neubauer, Magnetic fields at Jupiter, Science, 246, 1473, 1989.
- Russell, C.T., E.Chou, J.G. Luhmann, P. Gazis, L.H. Brace, and W.R. Hoegy, Solar and interplanetary control of the location of Venus' bow shock, J. Geophys. Res., 93, 5461, 1988.
- Russell, C.T., R.P. Lepping, and C.W. Smith, Upstream waves at Uranus, J. Geophys. Res., 95, 2273, 1990.
- Scarf, F.L., R.W. Fredericks, L.A. Frank, and M. Neugebauer, Nonthermal electrons and high-frequency waves in the upstream solar wind, 1, observations, J. Geophys. Res., 76, 5126, 1971.
- Scarf, F.L., and D.A. Gurnett, A plasma wave investigation for the Voyager mission, Space Sci. Rev., 21, 289, 1977.

Smith, C.W., and M.A. Lee, Coupled wave excitation and ion acceleration upstream of the Jovian bow shock, J. Geophys. Res., 91, 81, 1986.

Thomsen, M.F., Upstream suprathermal ions, in Collisionless Shocks in the Heliosphere: Reviews of Current Research, Ed. B.T. Tsurutani and R.G. Stone, AGU, p. 253, 1985.

Voigt, G.-H., and N.F. Ness, The magnetosphere of Neptune: its response to daily rotation, Geophys. Res. Lett., 17, 1705, 1990.

Zhang, T.-L., J.G. Luhmann, and C.T. Russell, The solar cycle dependence of the location and shape of the Venus bow shock, J. Geophys. Res., 95, 14961, 1990.

Figure Captions

Figure 1. The expected structure of Neptune's foreshock, showing the location of the electron and ion foreshocks with respect to the tangent magnetic field line, the bow shock, and each other. The figure also shows the expected time history of the Langmuir electric field E_L as a function of time along the spacecraft trajectory indicated (dotted line).

Figure 2. (a) Voyager plasma wave data showing all the Langmuir waves observed inbound to Neptune. These data are 20 second time-averaged. The waves are observed in primarily in the 562 Hz channel, with some spiky events in the 1.0 kHz and 311 Hz channels, in many bursts arranged in two main periods separated by 85 minutes. The existence of many clumps and peaks in the wave data implies multiple entries and exits into the foreshock. (b) Detailed, unaveraged, 562 Hz channel data. Several of the on/off (o) and peak (p) events selected for the remote-sensing analysis are indicated.

Figure 3. The three bottom panels show the B_X , B_Y , and B_Z components of the magnetic field (in nT) for the time period 1000 - 1400 SCET, day 236, 1989 during the inbound foreshock encounter. The top panel shows the 562 Hz PWS data on the same time scale. Wave events are clearly correlated with changes in the magnetic field direction. Note the large scale rotation of the field from 1115 - 1200 SCET which leads to disconnection of Voyager from the bow shock.

Figure 4. First evidence for large-scale motions of Neptune's bow shock. The shock surface shown is derived from the spacecraft positions and magnetic field directions for the wave events at 1115 and 1255 SCET. (The 1115 SCET magnetic field vector is tangent to the

shock near $Z = -8R_N$.) Voyager clearly should have crossed this shock very near 1255 SCET. This can be reconciled with the observed shock crossing only if large-scale motions of the shock occur.

Figure 5. Power spectra for the B_X , B_Y , and B_Z components from 1000 - 1400 SCET, showing the presence of strong spacecraft interference signals at frequencies up to and above 0.1 Hz.

Figure 6. Plots of the relations between a_s and b_s given by equation (3) for the 20 magnetic field vectors comprising the on/off PWS event from 1044:11 - 1044:51 SCET. Best-fit estimates for a_s and b_s are defined by the region of multiple intersections between the lines: $a_s = 46.6 \pm 0.2R_N$ and $b_s = 0.029 \pm 0.002R_N^{-1}$.

Figure 7. Similar to Figure 6 but for the peak event from 1101:03 - 1101:15 SCET. Best-fit estimates for the shock parameters are $a_s = 45.5 \pm 0.2R_N$ and $b_s = 0.027 \pm 0.002R_N^{-1}$. The least-squares analysis converges to $a_s = 45.6R_N$ and $b_s = 0.027R_N^{-1}$ for this event.

Figure 8. Time history of the a_s parameters determined by the remote-sensing analysis for all on/off events and many peak events observed inbound to Neptune. Both periods of wave activity show large-scale, monotonic decreases in a_s , corresponding to planetwards motion of the shock. The remote-sensing analysis indicates that the bow shock's nose moved from $46.6R_N$ to $34.3R_N$ during this period. The inbound shock crossing occurred at $X \sim 34.0R_N$, consistent with the extrapolated a_s values given by the remote-sensing analysis. Arrows show the a_s parameters of the MAG and PLS models.

Figure 9. Time history of the b_s parameters determined by the remote-sensing analysis in the

same format as Figure 8. Both periods of wave activity have approximately constant values of b_s ; these values differ by a factor close to 10 between the two wave periods. In comparison, the MAG and PLS shock models have $b_s \sim 0.008R_N^{-1}$ and $b_s \sim 0.010R_N^{-1}$, respectively. These values are bracketed by the remotely-sensed values.

Figure 10. Comparison of shock shapes inferred from the remote-sensing analysis and the MAG and PLS models. The 1045 SCET shock shape is significantly elongated and narrow compared with the blunt shock shapes characteristic after 1255 SCET. The MAG and PLS shocks lie between the 1045 SCET and 1440 SCET shock shapes for $X < 10R_N$.

Figure 11. Time variations in the position of the tangent point (small circles) and the spacecraft (solid line). Each circle shows the average X , Y or Z positions of the tangent point for a particular wave event, as determined by the remote-sensing analysis. The clustering of the circles near to, but both above and below, the spacecraft trajectory means that magnetic field variations caused the tangent point to flicker almost continuously from one side to the other of the spacecraft.

Figure 12. Comparison of the time histories of the L and M mode ram pressure data from the PLS instrument and the remotely-sensed time variations in a_s . The solar wind ram pressure increased by a factor of 3.2 from an unusually low level prior to about 1045 SCET to a constant (and typical) level after about 1200 SCET. The monotonic planetwards trend in the a_s values for the 1040 -1115 SCET period of wave activity is qualitatively and quantitatively consistent with ram pressure variations causing the observed shock location and motion. However, the ram pressure is constant (within 15%) during the second period of wave activity: the large-scale planetwards motion of the shock at these times cannot be

due to ram pressure variations. Instead, these shock motions are interpreted as evidence for Neptune’s rotational phase controlling the location of the bow shock.

Figure 13. Theoretical predictions for the relative shock nose position a_{th}/a_0 based on equation (6) and the L and M mode PLS data are shown using the circle and triangle symbols, respectively. The a_0 parameter is the average (theoretical) nose position after 1300 SCET. The black circles with error bars show the remotely-sensed a_s parameter normalized by the value $38.2R_N$ appropriate to 1300 SCET. Good qualitative and quantitative agreement between the calculated and remotely-sensed relative nose locations is evident for the period 1040 - 1115 SCET. This implies that the remote-sensing analysis is working correctly and argues strongly that the inferred variations in a_s do indeed correspond primarily to shock motions and not to changes in the shock’s orientation. The slightly different time variations in a_{th} and a_s in this period are interpreted in the text in terms of sunwards motion of the “base” shock. Finally, solar wind ram pressure and Mach number variations are qualitatively and quantitatively unable to account for the monotonic decrease in a_s for the period 1240 - 1430 SCET. These variations are interpreted instead in terms of Neptune’s rotation phase controlling the location of the bow shock.

Figure 14. The bottom panel shows the time history of the nose location a_c of the shock normalized for the observed variations in ram pressure and Mach number using equation (6) and the PLS data. The “base” shock moves sunwards from 1040 - 1115 SCET and planetwards from 1300 - 1430 SCET, with a maximum standoff distance in the period 1115 - 1230 SCET. The top panel shows the (Neptunian) magnetic latitude and longitude of the Sun with full and dashed lines, respectively. The peak in a_c occurs while Neptune’s

magnetic dipole is nearly perpendicular to the solar wind flow and the Sun's magnetic longitude is in the range $0 - 57^\circ$.

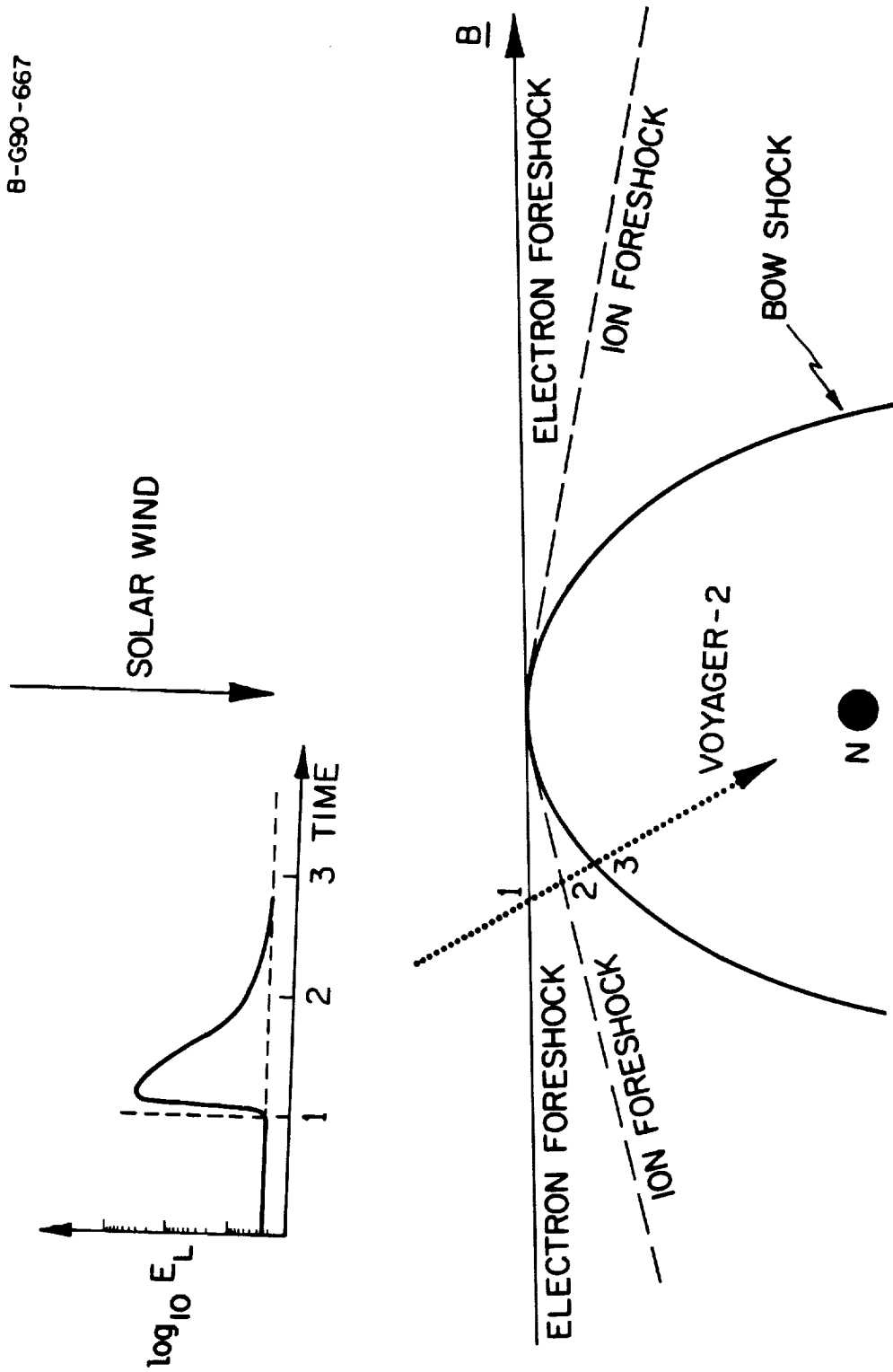


Figure 1

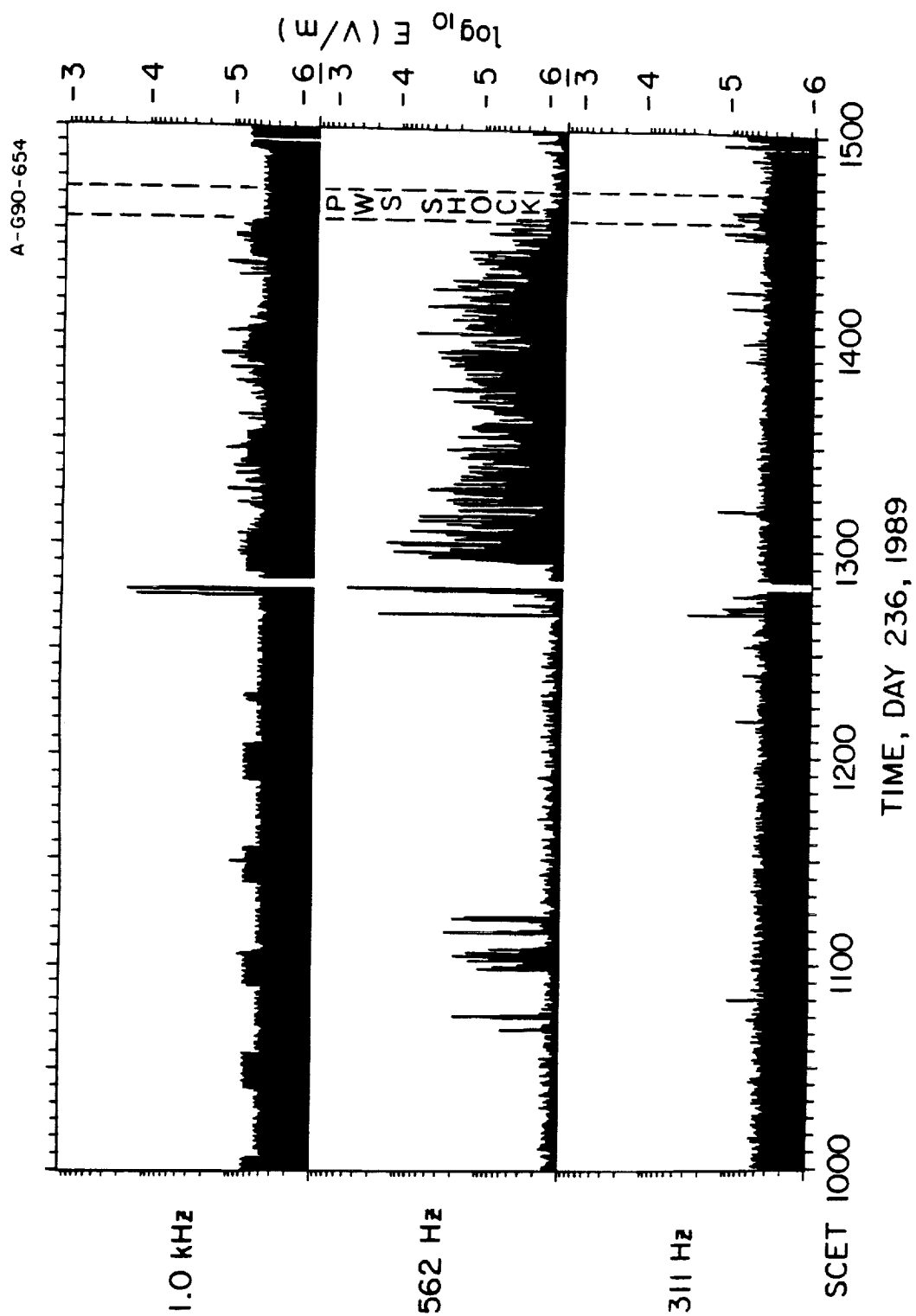


Figure 2a

B-G90-656

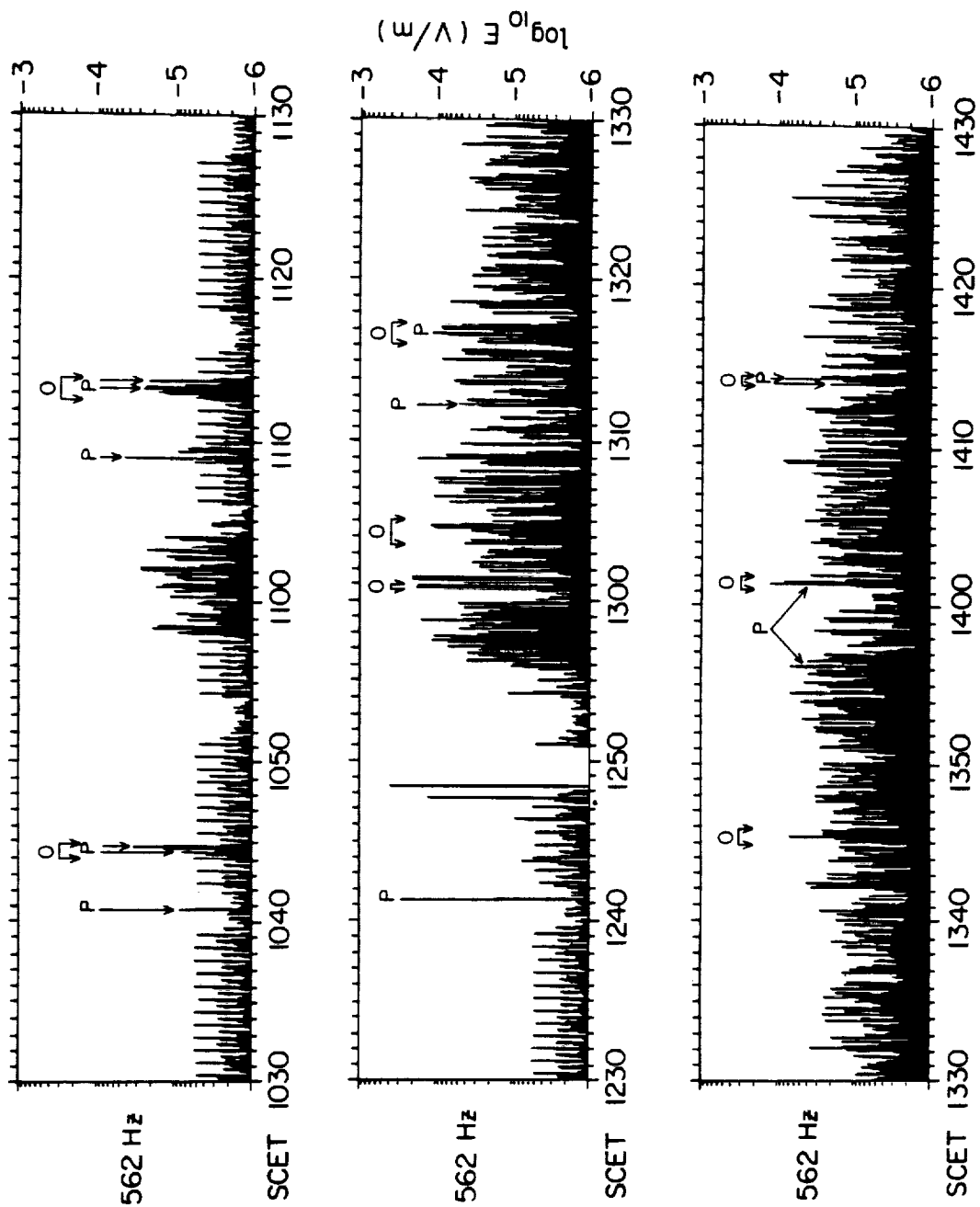


Figure 2b

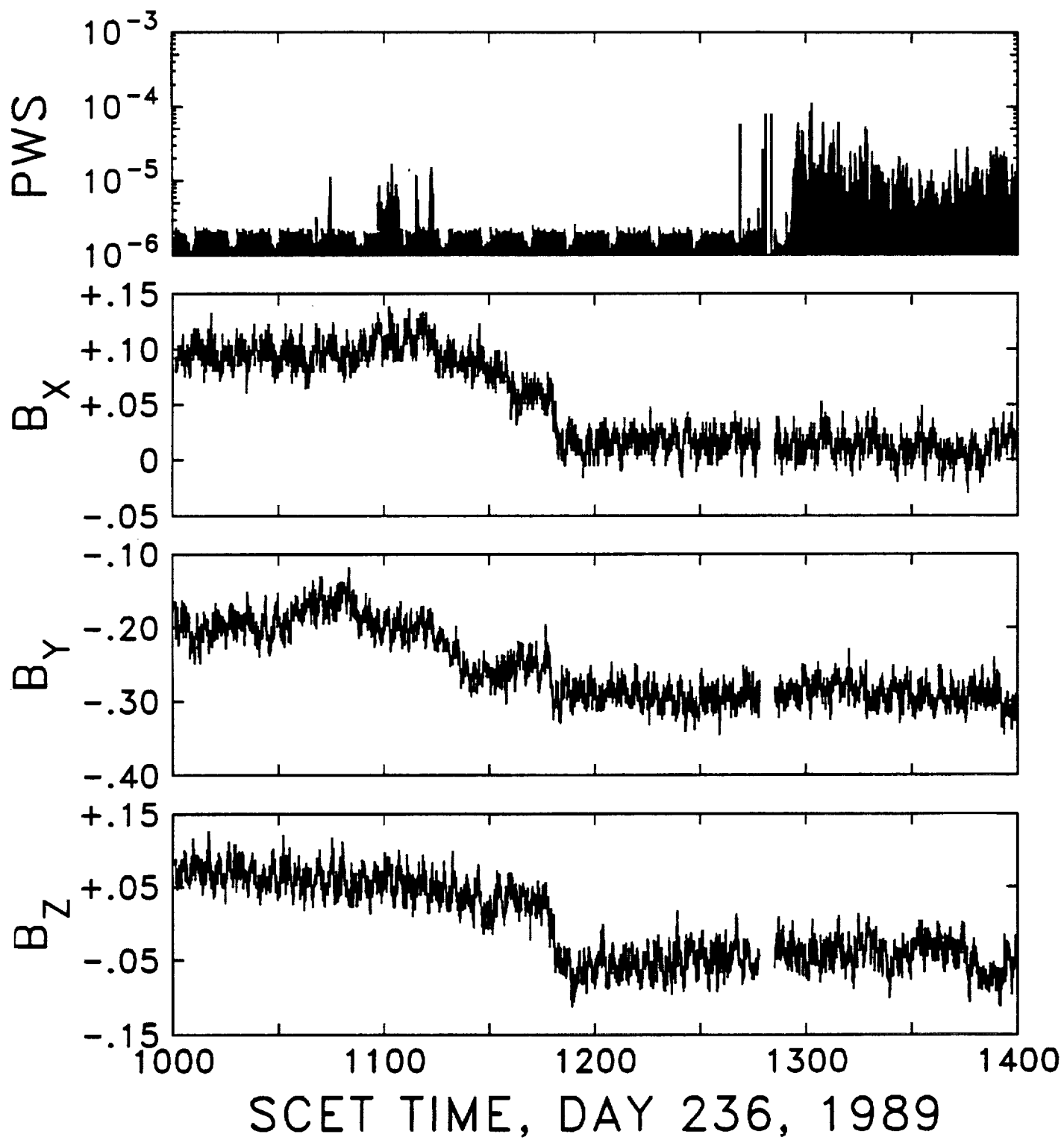


Figure 3

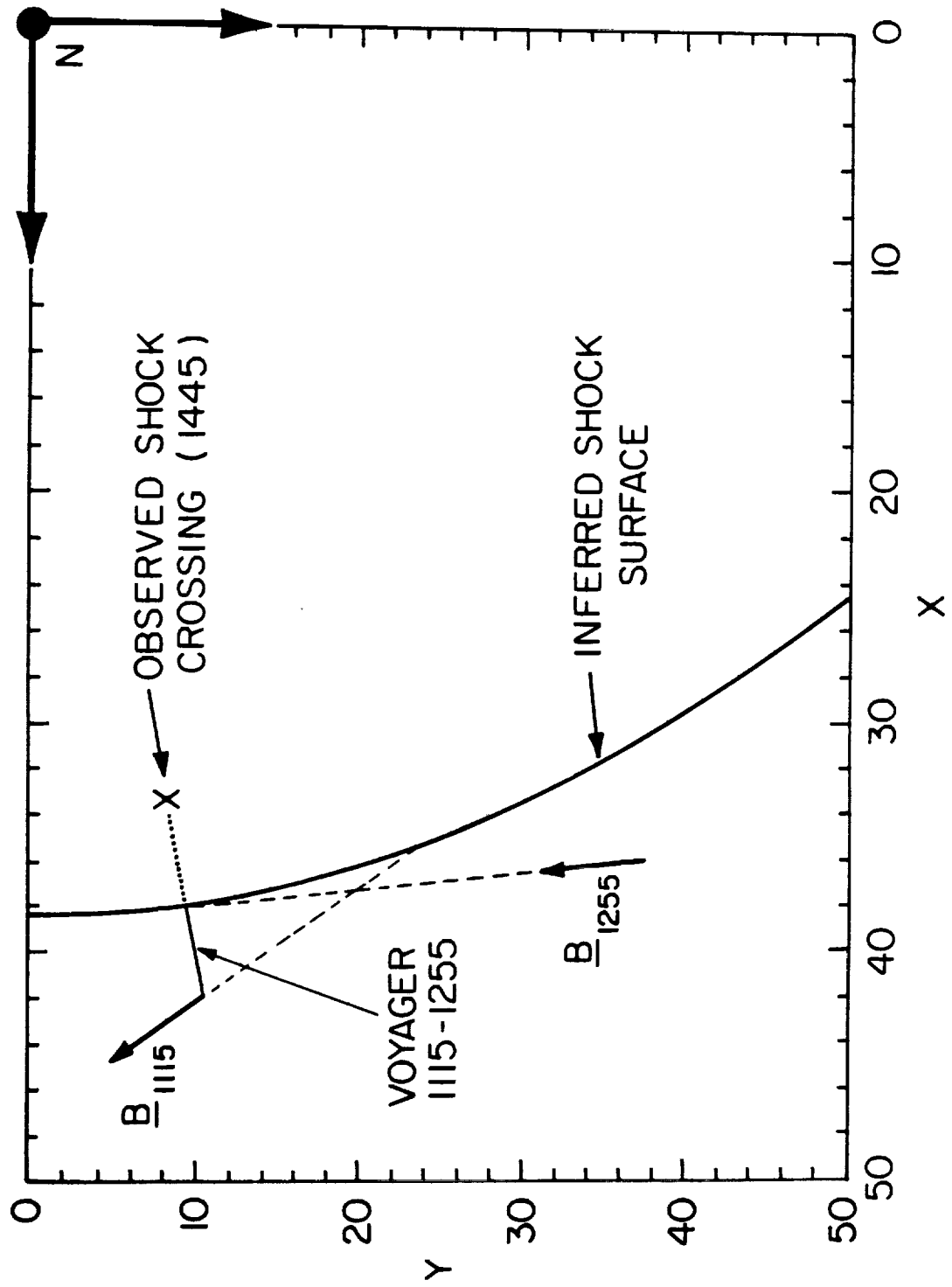


Figure 4

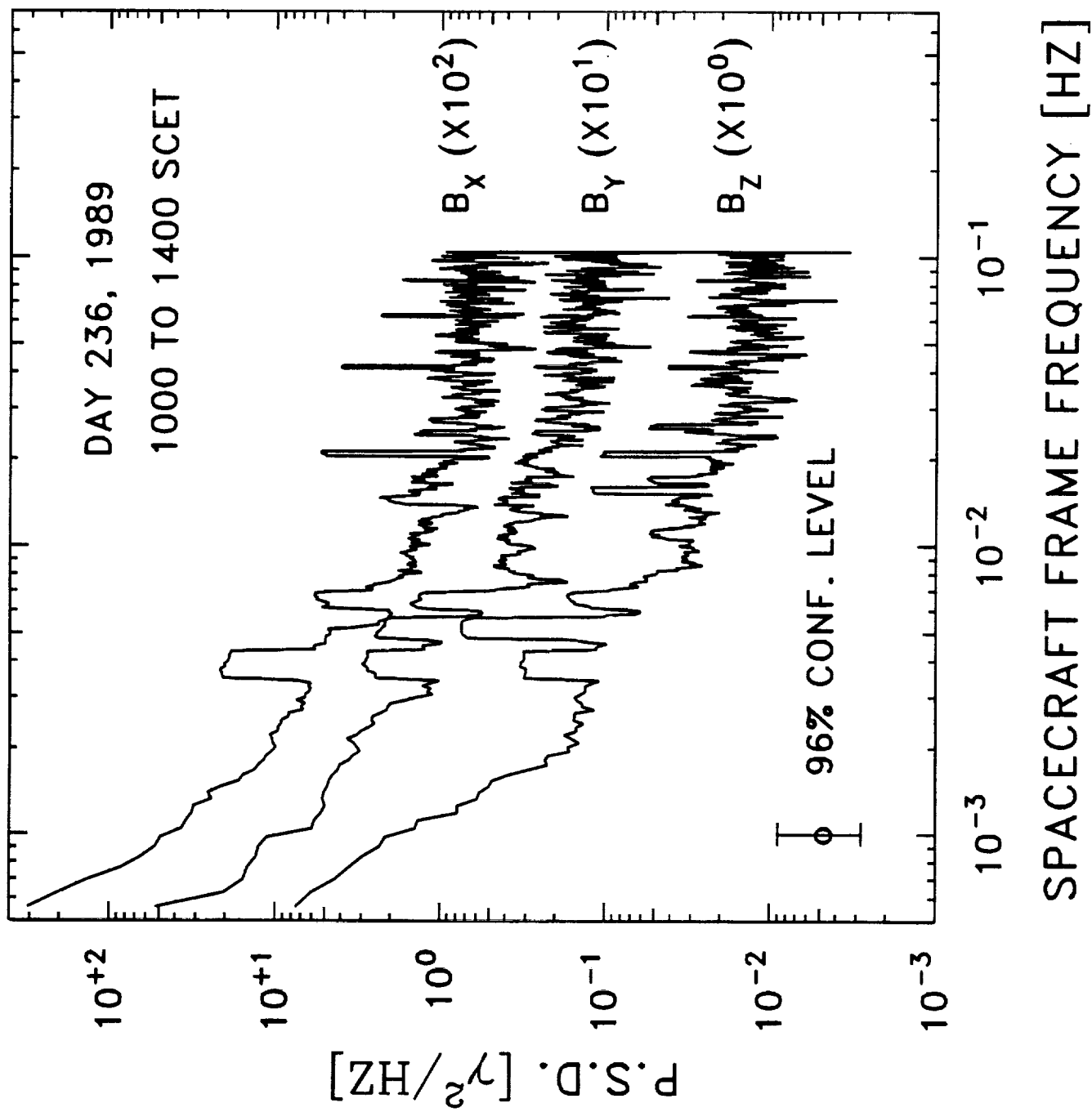


Figure 5

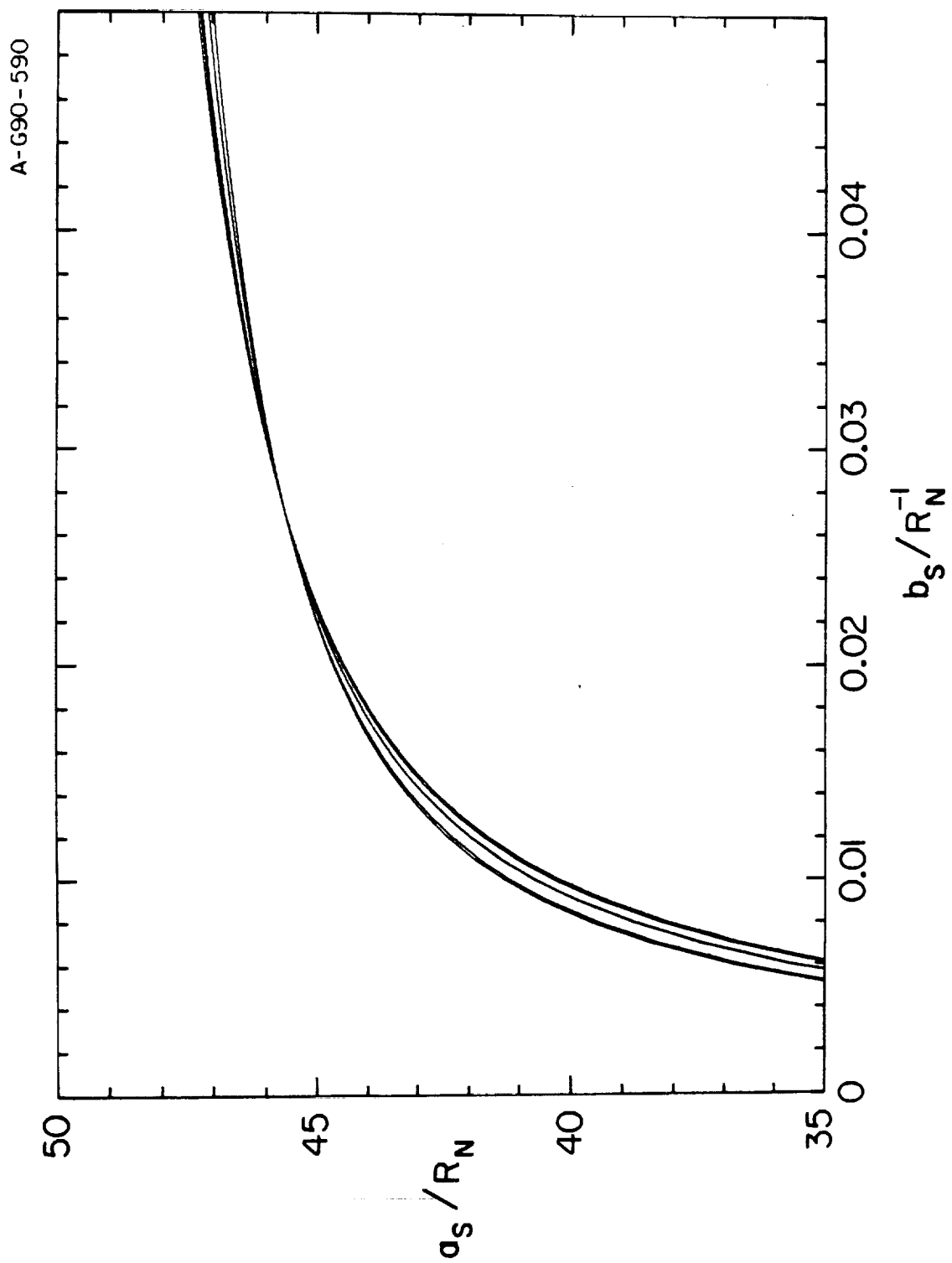


Figure 6

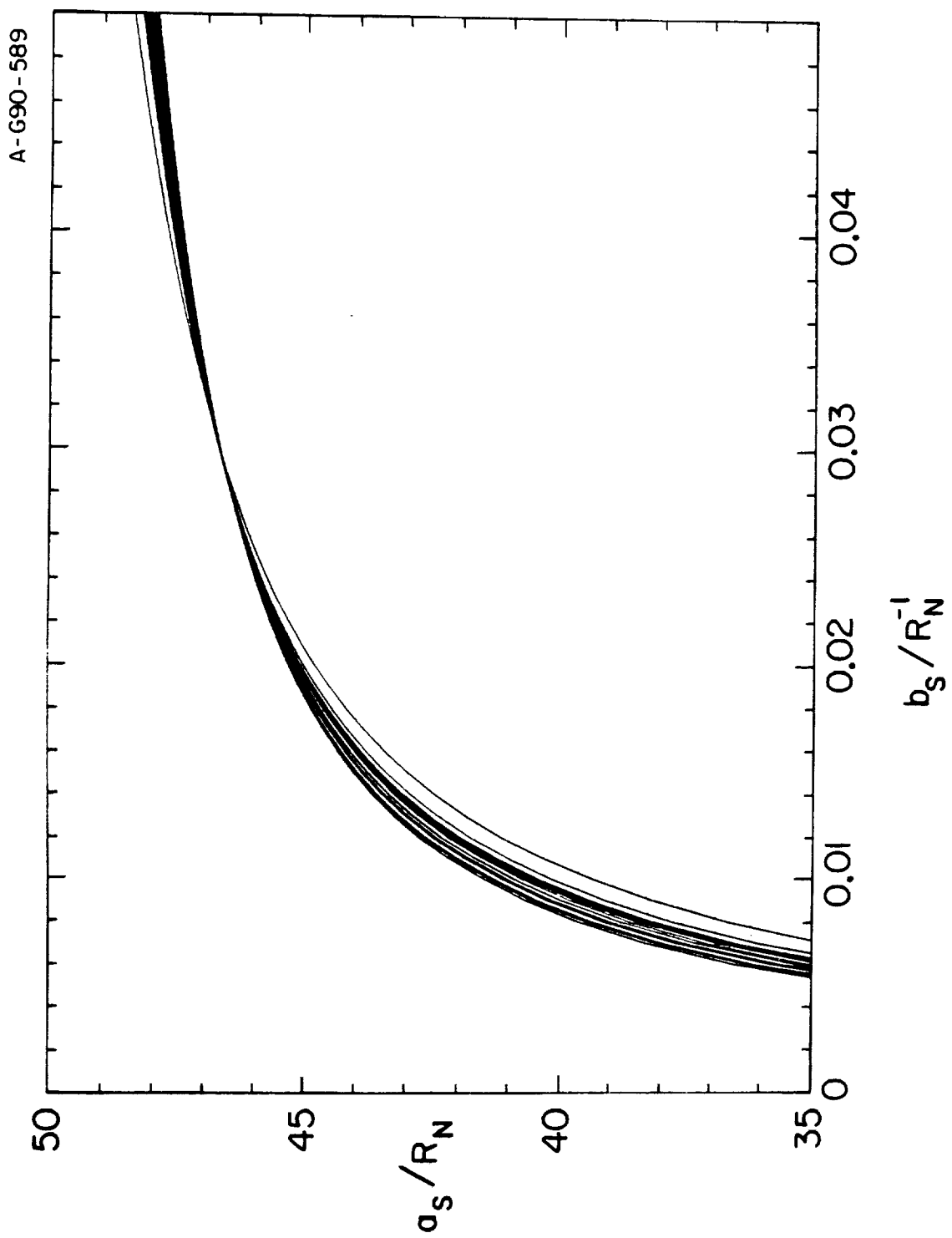


Figure 7

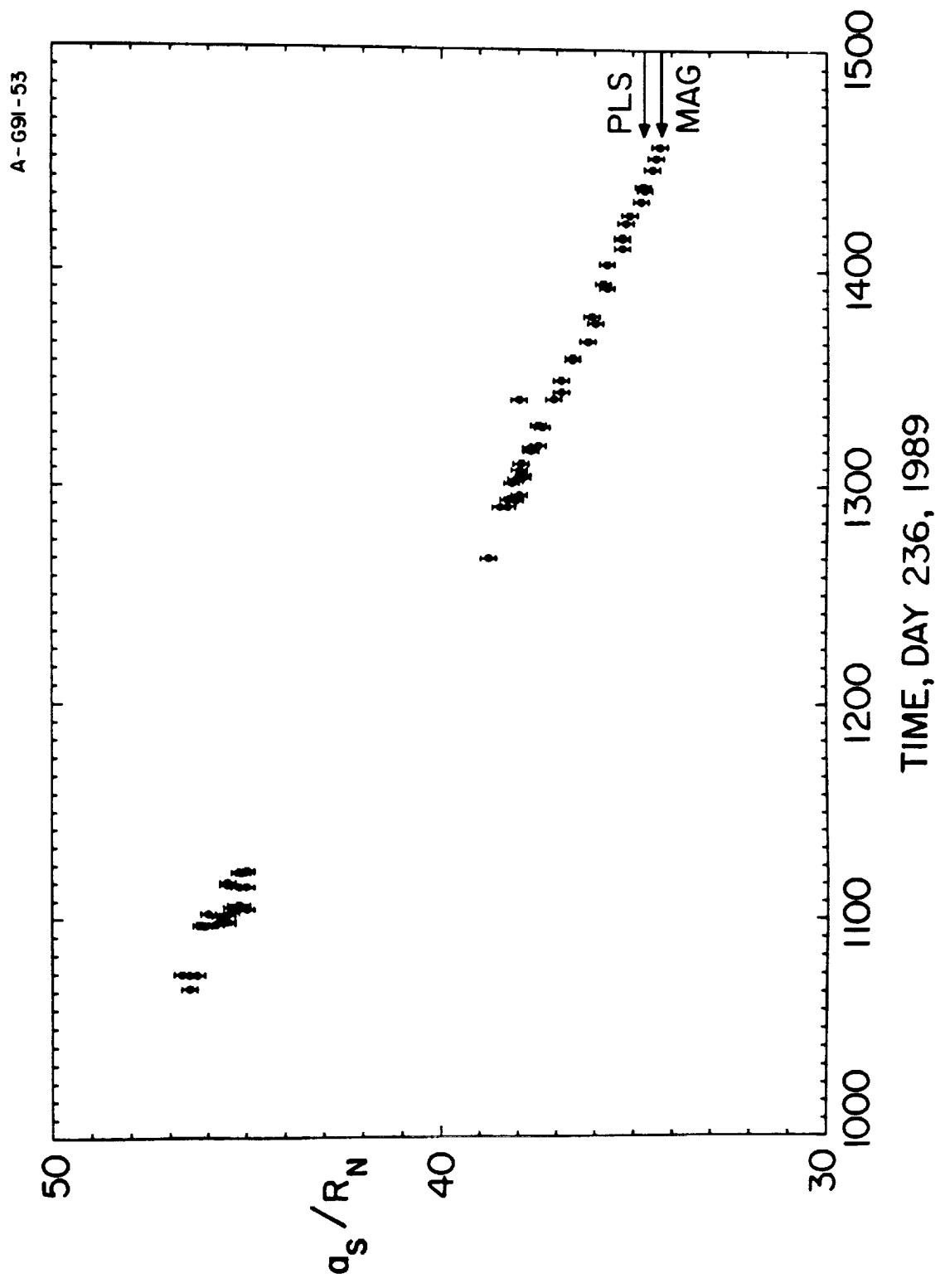


Figure 8

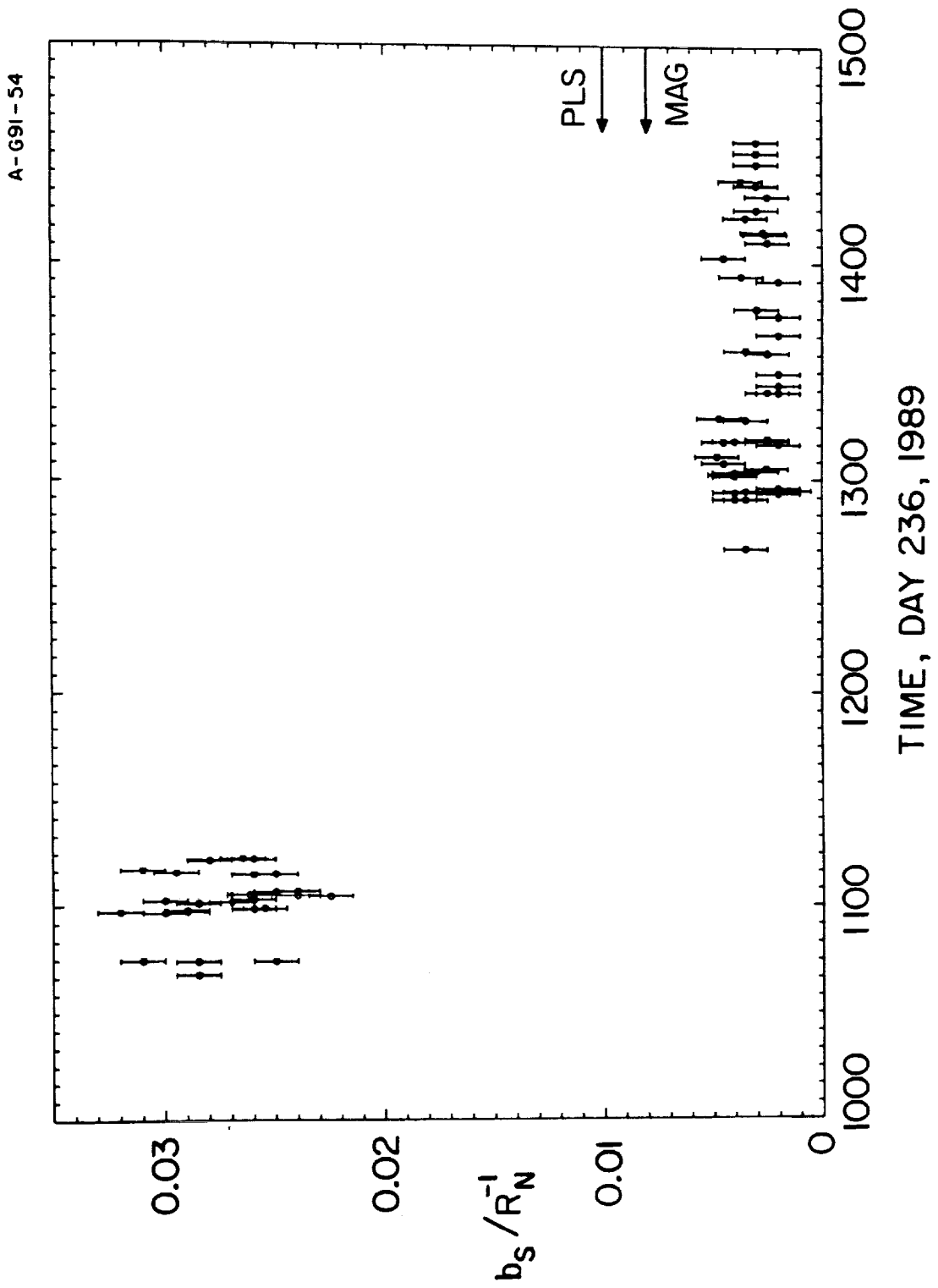


Figure 9

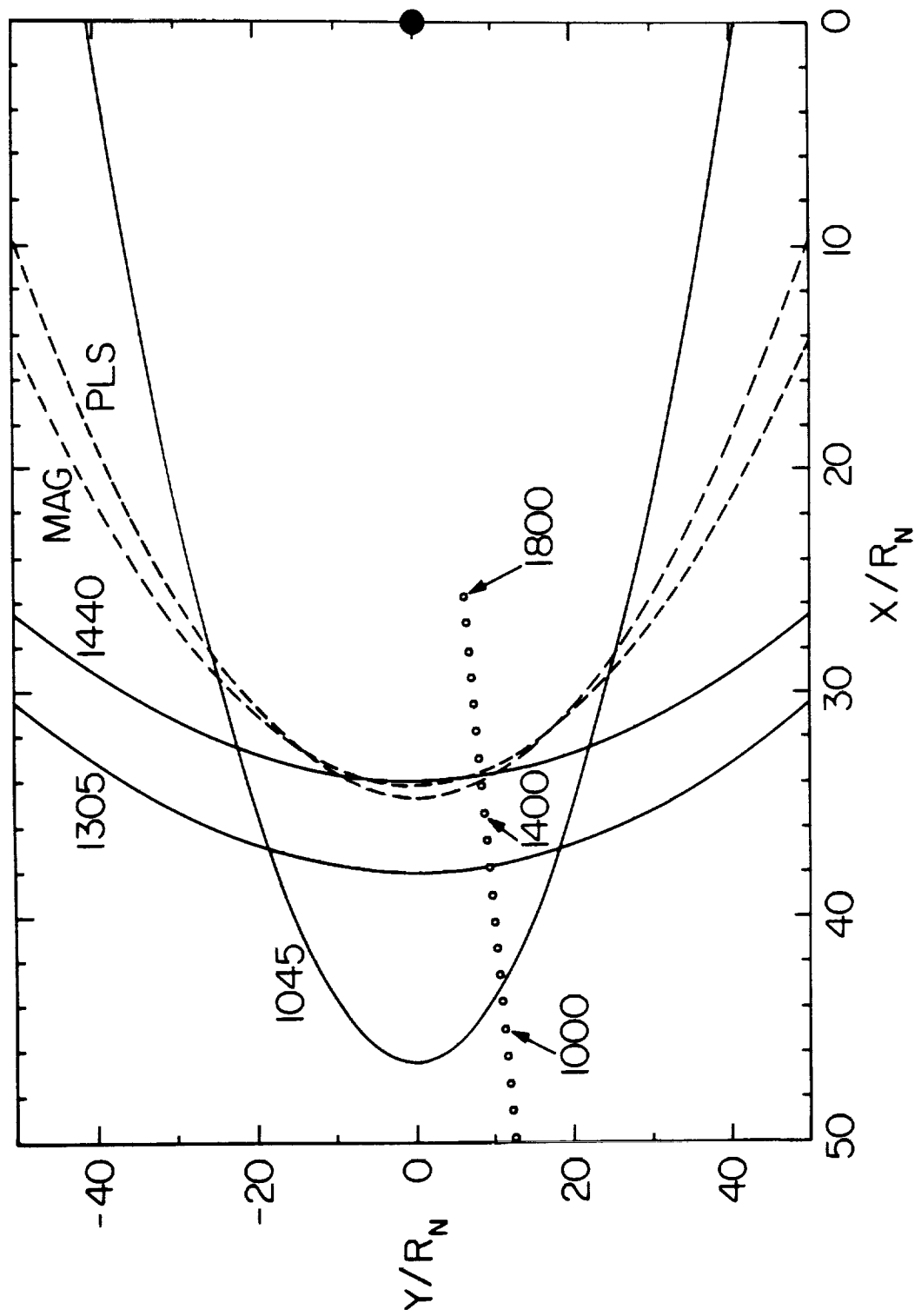


Figure 10

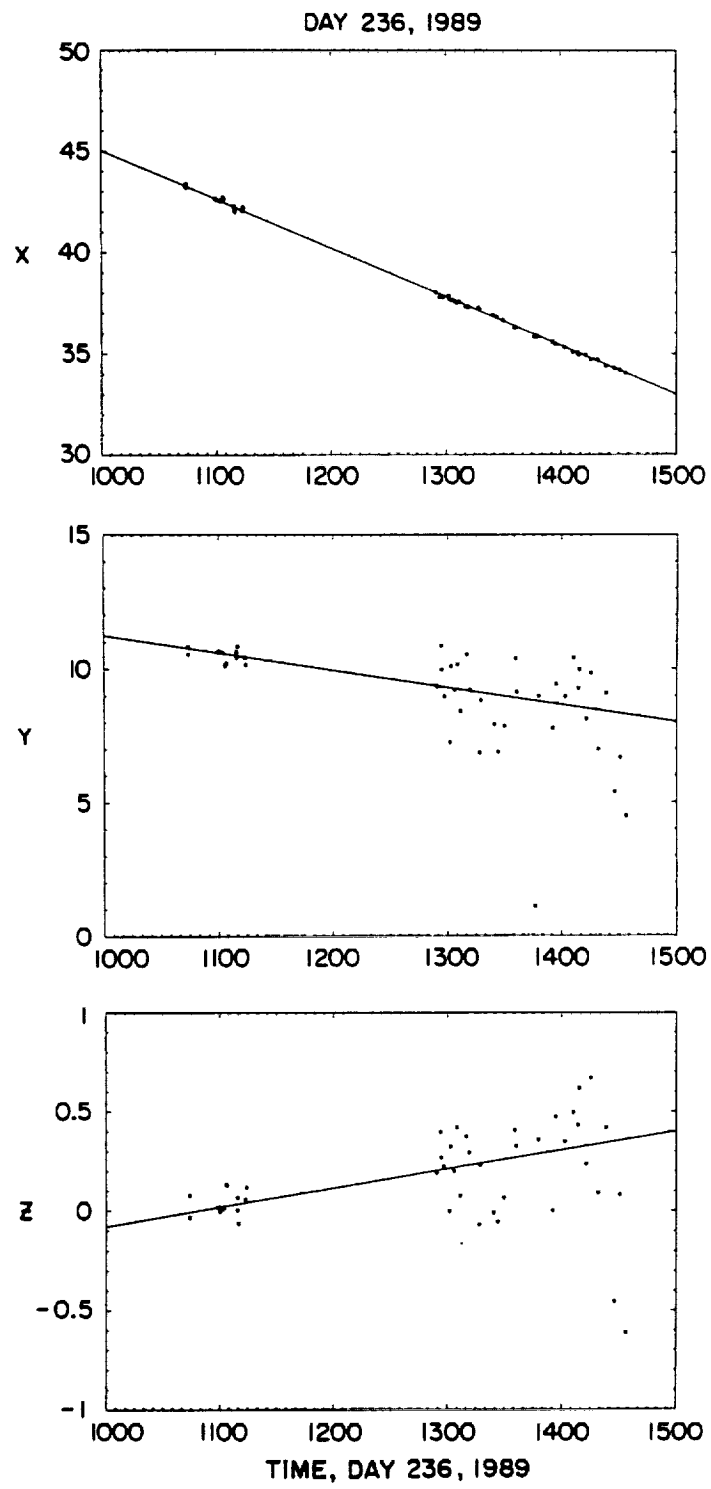


Figure 11

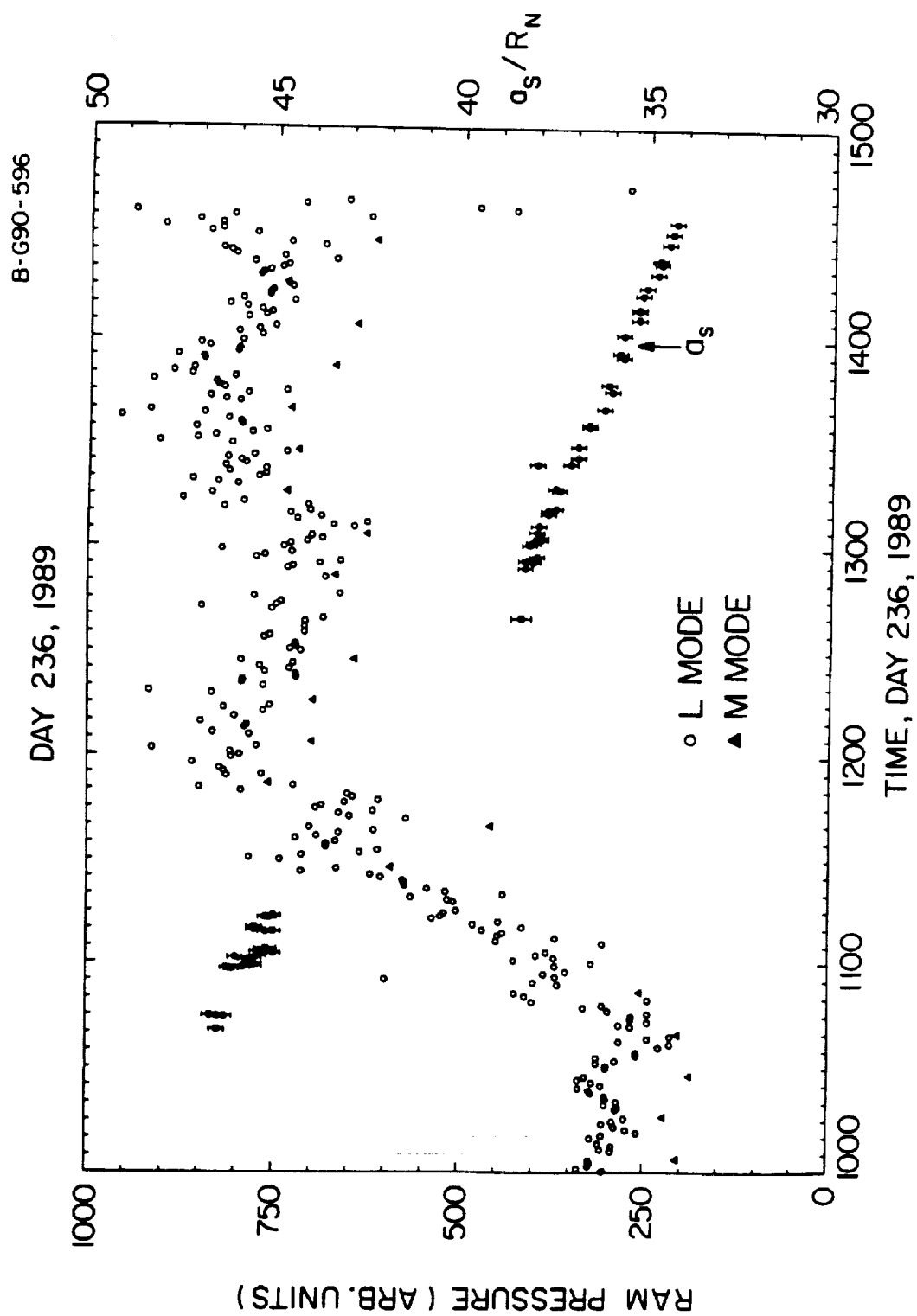


Figure 12

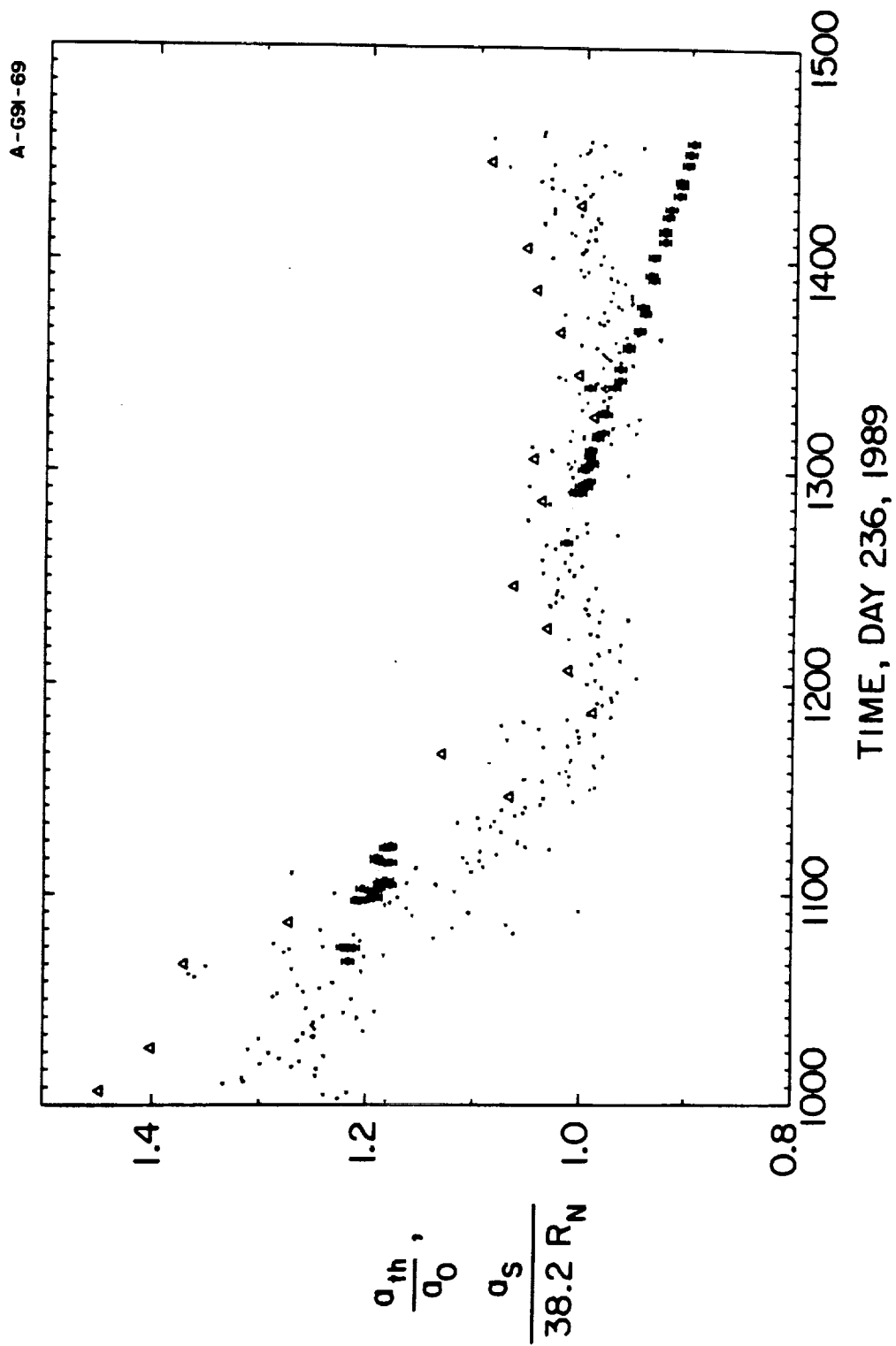


Figure 13

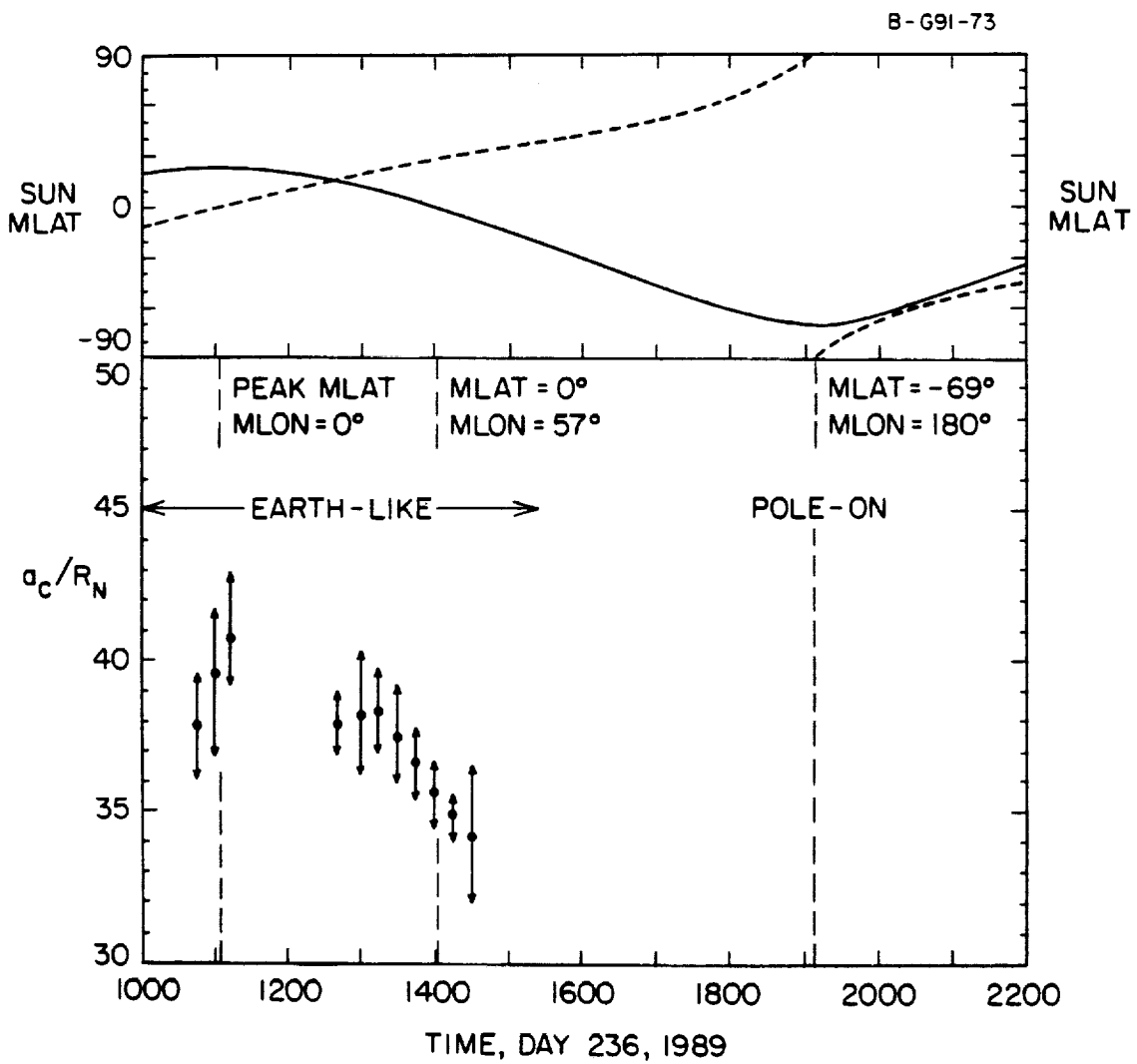


Figure 14

